Observational constraints on the fracture energy of subduction zone earthquakes

Anupama Venkataraman[1] and Hiroo Kanamori
Seismological Laboratory, California Institute of Technology, Pasadena, California, USA

Received 21 April 2003; revised 28 October 2003; accepted 10 February 2004; published 11 May 2004.

[1] We relate seismologically observable parameters such as radiated energy, seismic moment, rupture area, and rupture speed to the dynamics of faulting. To achieve this objective, we computed the radiated energy for 23 subduction zone earthquakes recorded between 1992 and 2001; most of these earthquakes have a magnitude $M_w > 7.5$, but we also included some smaller ($M_w \sim 6.7$) well-studied subduction zone earthquakes and six crustal earthquakes. We compiled static stress drop estimates for these 29 earthquakes from literature and used a slip-weakening model to determine the radiation efficiency of these earthquakes. We also determined the rupture speed of these earthquakes from literature. From fracture mechanics, fracture energy, and hence radiation efficiency, can be related to the rupture speed. The radiation efficiencies estimated from the partitioning of energy as given by the slip-weakening model are consistent with the rupture speed estimated for these earthquakes. Most earthquakes have radiation efficiencies between 0.25 and 1 and are hence efficient in generating seismic waves, but tsunami earthquakes and two deep earthquakes, the 1994 Bolivia and the 1999 Russia-China border earthquakes, have very small radiation efficiencies (<0.25) and hence dissipate a large amount of energy during faulting. We suggest that differences in the radiation efficiencies of different types of earthquakes could be due to fundamental differences in their rupture mechanics. In deep events, the energy is probably dissipated in thermal processes in the fault zone, while it is possible that the morphology of the trench causes large energy dissipation during the rupture process of tsunami earthquakes. *INDEX TERMS:* 7209 Seismology: Earthquake dynamics and mechanics; 7215 Seismology: Earthquake parameters; 7230 Seismology: Seismicity and seismotectonics; *KEYWORDS:* radiation efficiency, fracture energy, dissipated energy, rupture velocity, static stress drop, radiated seismic energy

Citation: Venkataraman, A., and H. Kanamori (2004), Observational constraints on the fracture energy of subduction zone earthquakes, *J. Geophys. Res.*, *109*, B05302, doi:10.1029/2003JB002549.

1. Introduction

[2] Subduction zones, regions on the earth where one plate slides beneath another, host a whole suite of earthquakes—interplate, tsunami, intraplate, and deep earthquakes. The different types of subduction zone earthquakes have differences in the frequency content of the seismic energy released. For example, tsunami earthquakes [*Kanamori*, 1972; *Polet and Kanamori*, 2000] occur in the shallow portions of the subduction zone. Compared to ordinary subduction zone earthquakes, tsunami earthquakes are deficient in high-frequency energy; however, they have a significant amount of slip. Thus they produce relatively minor shaking, but are followed by destructive tsunamis that are much larger than expected from the seismic moment. Are these differences between tsunami earthquakes and regular plate-interface earthquakes due to differences in their rupture mechanisms? To understand this, we investigate the rupture mechanics of the different types of subduction zone earthquakes, using macroscopic source parameters— radiated seismic energy (E_R), seismic moment (M_0), rupture area (S) and rupture velocity (V). In particular, we attempt to place constraints on the fracture energy (E_G) associated with these earthquakes because fracture energy is an important quantity in understanding fracture mechanics. The advantage of using such macroscopic parameters is that we can investigate the overall frictional conditions on the fault even if the details of the rupture processes are not known [*Kanamori and Heaton*, 2000].

[3] In this paper, we computed teleseismic estimates of radiated energy for 23 large subduction zone earthquakes; most of these earthquakes have magnitude $M_w > 7.5$, but we also included some smaller well-studied subduction zone earthquakes. For comparison, we studied six crustal earthquakes. We compiled the static stress drop estimates and rupture velocities for these 29 earthquakes from literature. From the seismic moment, radiated energy and static stress drop, we calculated the fracture energy and radiation

[1]Now at Department of Geophysics, Stanford University, Stanford, California, USA.

0148-0227/04/2003JB002549$09.00

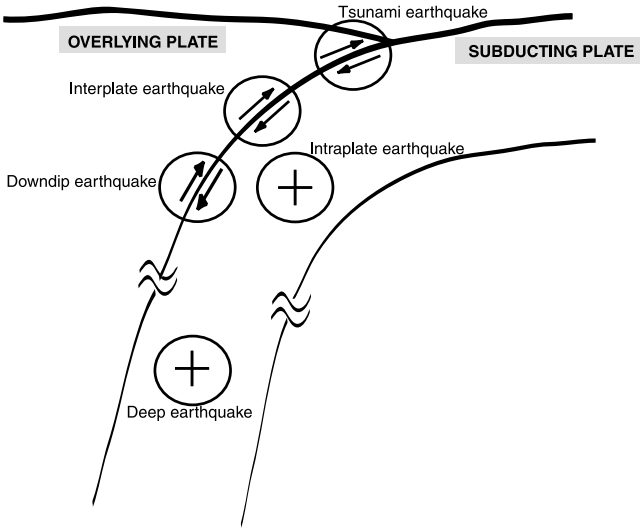

Figure 1. Cartoon showing the location of the different types of subduction zone earthquakes relative to the subducting slab.

efficiency for these earthquakes and interpreted our results in the light of differences in rupture mechanics.

2. Different Types of Subduction Zone Earthquakes

[4] Depending on the location of the earthquakes relative to the subducting slab, we classified subduction zone earthquakes as shown in Figure 1: Type 1, plate interface (interplate) earthquakes, which occur at the interface between the overlying plate and the subducting plate (i.e., typical subduction zone earthquakes; e.g., the 1995 Chile earthquake); Type 2, tsunami earthquakes, which occur at shallow depths in the slab and produce tsunamis much larger than are expected from their seismic moment (e.g., the 1992 Nicaragua earthquake); Type 3, downdip earthquakes—in this category we grouped earthquakes that rupture downward along the dip of the subducting slab (such as the 1994 Sanriku earthquake) and earthquakes that rupture the bottom portion of the known seismogenic zone (like the 1997 Kamchatka earthquake); Type 4, intraplate earthquakes, which occur within the subducting slab at depths less than 250 km (e.g., the 2001 Nisqually earthquake); and Type 5, deep earthquakes (e.g., the 1994 Bolivia earthquake), which occur within the subducting slab at depths greater than 500 km [*Gutenberg and Richter*, 1938, 1939].

[5] In addition to these subduction zone earthquakes, we included Type 6, crustal earthquakes (not shown in the figure), which occur in continental crust (e.g., the 1999 Hector Mine earthquake); these were included because many of them are well studied using regional arrays and hence serve as useful and important comparisons.

3. Radiated Energy of Subduction Zone Earthquakes

[6] To estimate the radiated energy from 23 well-recorded subduction zone earthquakes that occurred between 1992 and 2001 (shown on the location map in Figure 2), we used *P* wave teleseismic data recorded at broadband stations around the world and archived at the IRIS Data Management Center. Only the vertical component data (BHZ channel) of stations at distances between 30° and 90° were used in this study. We applied corrections for path and radiation pattern [*Boatwright and Choy*, 1986], to determine the moment rate spectrum ($\dot{M}(f)$) from the displacement spectrum ($\hat{u}(f)$) at a station using

$$|\hat{\dot{M}}(f)| = \frac{4\pi\rho^3 v_{\alpha,\beta}^3 R_E e^{(\pi f t^*)} |\hat{u}(f)|}{g(\Delta) R(\theta,\phi) C |\hat{I}(f)|},$$

where at teleseismic distances the geometric spreading factor $1/r$ is replaced by $g(\Delta)/R_E$, $R_E = 6371$ km is the radius of the earth, $v_{\alpha,\beta}$ is the *P* wave or *S* wave velocity, t^* is the attenuation factor (equal to the travel time divided by the path-averaged *Q* factor), *C* is the free surface receiver effect, and $\hat{I}(f)$ is the instrument response. By integrating the squared moment rate spectrum determined at each station we computed radiated energy, E_R. Thus

$$E_R = \left[\frac{8\pi}{15\rho\alpha^5} + \frac{8\pi}{10\rho\beta^5}\right] \int_0^\infty f^2 |\hat{\dot{M}}(f)|^2 df,$$

where ρ is the density, and α and β are the *P* and *S* wave velocities of the medium. We refer to this method of estimating radiated energy as the single-station method. The first and the second terms in the parenthesis on the right-hand side of the equation represent contributions from *P* and *S* waves, respectively; the *P* wave contribution is about 5 percent of the *S* wave contribution. The mean value of these single-station estimates is the total *P* wave energy of the earthquake and the *S* wave energy is determined from the *P* wave energy, using the *S* to *P* wave energy ratio [*Venkataraman and Kanamori*, 2004]. Figure 3 shows the *P* wave energy spectral density for the 2001 India earthquake. Most of the energy is around the corner frequency (~0.05 Hz) and falls off rapidly with frequency (best fit slope of displacement spectra ~1.9). About 88% of the energy is included in the frequency band of integration (up to 1 Hz).

[7] The details of the path corrections applied to the velocity spectrum are described by *Venkataraman and Kanamori* [2004], but we briefly mention a few important points here. For shallow events, the depth phases cannot be separated from the direct phase, so the *P* wave group (which includes the direct *P*, *pP* and *sP*) is used to compute radiated energy; for deeper events, only the direct *P* wave is used. The single-station estimate of energy does not account for directivity effects resulting from source finiteness. The effect of directivity on radiated energy estimates depends on the slip time history and station distribution [*Venkataraman and Kanamori*, 2004]. From our computations, we observe that the directivity corrections for dip-slip earthquakes with rupture along strike alter the teleseismic energy estimates by less than a factor of 2; hence we do not include these corrections in our final estimates of teleseismic energy from subduction zone earthquakes. However, directivity could have a significant effect on the teleseismic energy estimates of crustal strike-slip earthquakes; for these earthquakes we

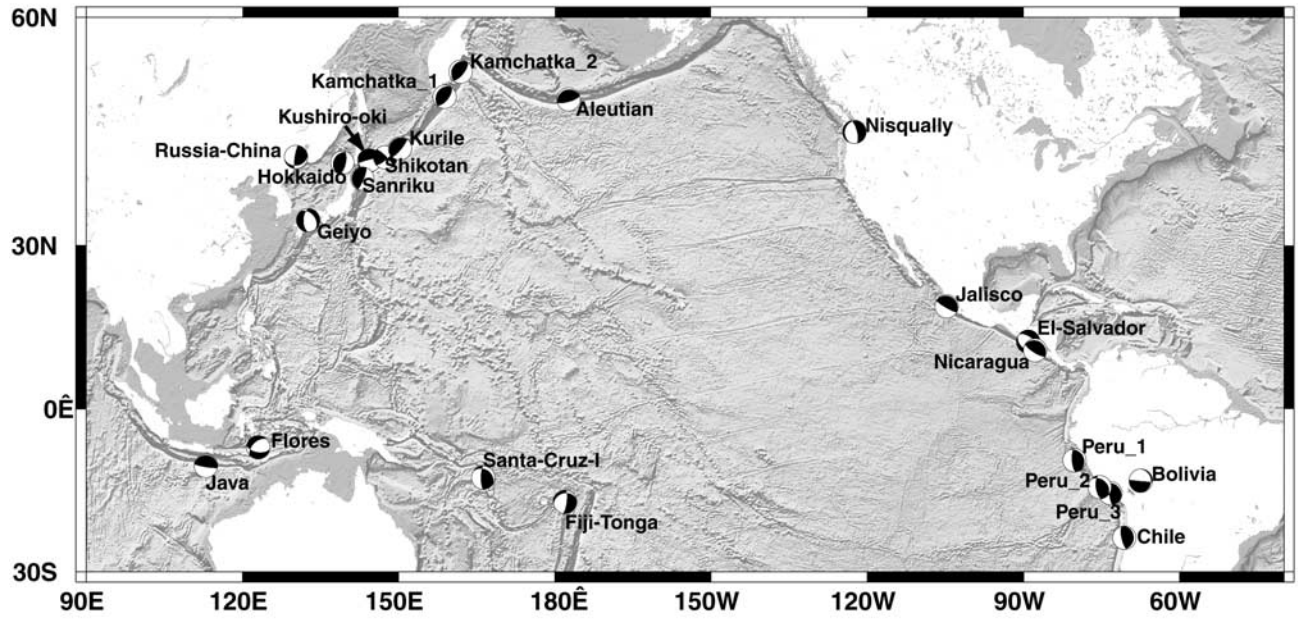

Figure 2. Map showing the location and focal mechanism of 23 large (mostly $M_w > 7.5$) subduction zone earthquakes studied here.

include corrections for directivity obtained using slip models when such models are available.

[8] Figure 4 shows the single-station teleseismic radiated energy estimates of six earthquakes—one of each type in our classification. The energy estimates of the other earthquakes are listed by *Venkataraman* [2002]. For each earthquake, the plot on the left shows the single-station energy estimates at individual stations (the stations are arranged in order of increasing radiation pattern) and, the plot on the right shows the azimuthal distribution of stations. We rejected stations with low signal-to-noise ratio and stations close to the *P* node (radiation pattern coefficients less than 0.2). Small amplitudes of the *P* wave group at nodal stations results in low signal-to-noise ratios; moreover, the arrival of scattered energy at these stations could potentially bias the radiated energy estimates. Below each plot, we include a brief description of the earthquake highlighting its important characteristics. Several earthquakes have poor azimuthal station distribution; however, this should not significantly affect the average radiated energy estimates because most of these earthquakes have a dip-slip mechanism with rupture propagating along strike and hence the directivity effects are small. The radiated energy for the January 17, 1994, Northridge earthquake is the regional estimate (see footnote, Table 1), and the radiated energy for the October 16, 1999, Hector Mine earthquake was determined as given by *Venkataraman et al.* [2002] and corrected for directivity as shown by *Venkataraman and Kanamori* [2004].

[9] The open diamonds in Figure 4 represent the radiated energy estimates obtained by time domain integration of the squared velocity records. While the time domain estimates are not corrected for attenuation, the frequency domain estimates of energy (solid circles) include an attenuation correction. The time domain estimates are useful in choosing the appropriate time window of the record such that most of the *P* wave group energy arrives within this window, and the effect of scattered energy on the energy estimates is minimized. Since the time domain estimates do not correct for attenuation, they represent the lower limit of the radiated energy for each earthquake and the difference between the time domain and frequency domain estimates reflects the effect of the attenuation correction on the radiated energy estimates. The frequency domain estimates include all the energy in frequencies up to 1 Hz; for most of the earthquakes studied here, less than 25% energy is at frequencies larger than 1 Hz and hence this was not included in the final energy estimates.

[10] In Table 1, the mean and median of the single-station estimates of radiated energy in the frequency domain are listed. For most of the earthquakes listed in Table 1, the mean is within a factor of two of the median. If we consider directivity effects, the mean energy is more representative of the total radiated energy of an earthquake; thus we use the mean energy estimates in our study. The energy to moment ratio as function of moment magnitude is shown in Figure 5. From Figure 5 we observe that the radiated energy-to-moment ratio is different for different types of earthquakes; tsunami earthquakes have the smallest radiated energy-to-moment ratio (7×10^{-7} to 3×10^{-6}), interplate and downdip earthquakes have a slightly larger ratio (5×10^{-6} to 2×10^{-5}) and intraplate and deep earthquakes have ratios similar to crustal earthquakes (2×10^{-5} to 3×10^{-4}). The energy to moment ratios for some of these earthquakes have been estimated by *Choy and Boatwright* [1995] and by NEIC, and our estimates differ from these results by less than a factor of 3.

4. Partitioning of Energy in Earthquakes

4.1. Slip-Weakening Model

[11] Figure 5 shows that $\tilde{e} = E_R/M_0$, the ratio of energy-to-moment (this is the energy scaled by the seismic moment,

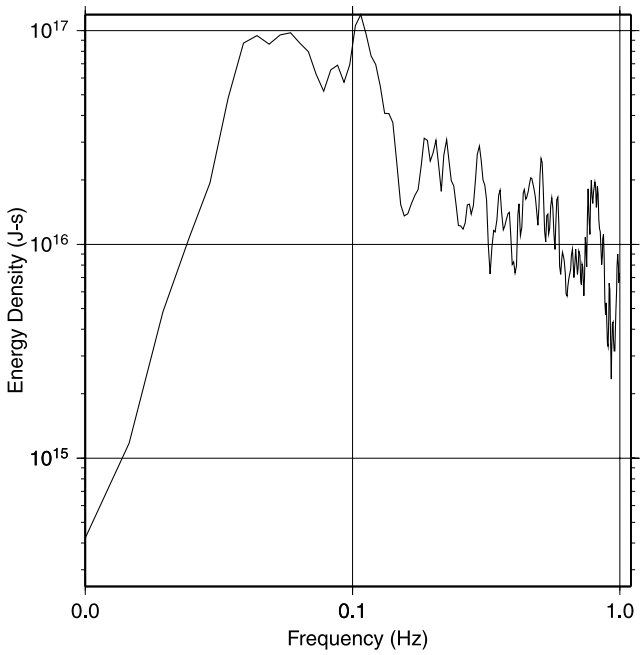

Figure 3. The *P* wave energy spectral density for the 2001 India earthquake. The frequency domain estimates include all the energy in frequencies up to 1 Hz; in most of the earthquakes studied here, there is less than 25% energy at frequencies larger than 1 Hz, and hence this was not included in the final energy estimates.

and is also called the scaled energy) is different for different types of earthquakes. To relate these ratios to the physical processes in the fault zone, we have to understand the partitioning of energy in earthquakes. An earthquake is a stress relaxation process, during which the total potential energy (strain energy + gravitational energy) drops from W to $W - \Delta W$. The total potential energy change in an earthquake is given as $\Delta W = \overline{\sigma}\overline{D}S$ [*Knopoff*, 1958; *Dahlen*, 1977; *Kostrov*, 1974], where $\overline{\sigma}$ is the average stress during faulting, $\overline{D}$ is the average displacement on the fault and S is the rupture area. A part of the total potential energy is dissipated on the fault plane and is given as $\overline{\sigma}_f\overline{D}S$, where $\overline{\sigma}_f$ is the average frictional stress on the fault plane. The remaining part is radiated as seismic waves and the wave energy is known as radiated energy (E_R). Since this is a macroscopic representation of the earthquake process, all quantities are averaged over the fault plane. A more detailed explanation of the definitions of these quantities is included in Appendix A.

[12] During stress relaxation, the shear stress on the fault drops from an initial stress before the earthquake, to a final stress after the earthquake, as shown in Figure 6a. However, for any physically realistic model this stress drop is not instantaneous and occurs over a critical slip of D_c as shown in Figure 6b. The stress on the fault varies as a function of slip as given by σ_f and is shown by the dark curve in Figure 6b. In this model, when the fault slip exceeds the critical slip, the frictional stress remains constant and is equal to the final stress. This behavior in which the stress on the fault plane gradually decreases as slip increases is often called ''slip-weakening'' in literature [*Rice*, 1980; *Li*, 1987]. We can interpret this stress relaxation process (or slip-weakening process) in terms of creation of a breakdown zone at the advancing rupture front. Then, the total dissipated energy, $\overline{\sigma}_f\overline{D}S$, can be divided into two parts, the fracture energy, E_G, and heat energy, E_H, i.e., $\overline{\sigma}_f\overline{D}S = E_G + E_H$. Thus the total potential energy change can be written as $\Delta W = E_R + E_G + E_H$, while the radiated energy, can be written as

$$E_R = \frac{(\sigma_0 + \sigma_1)}{2}\overline{D}S - \overline{\sigma}_f\overline{D}S.$$

Thus the area under the trapezium (indicated by the dotted line) in Figure 6b represents the total potential energy released in an earthquake, ΔW. The radiated energy, as given by the above equation, is the striped area. The heat energy represented by the dotted area is given as $E_H = \sigma_{f0}\overline{D}S$. The fracture energy, E_G, represented by the area of the unshaded region, is the energy used in mechanical processes near the fault zone as the rupture propagates. Thus Figure 6b is a schematic representation of the partitioning of energy in earthquakes. This model, though simple at first glance, is general enough and includes all the essential features of partitioning of energy in earthquakes.

[13] Using this model, we can determine radiation efficiency [*Husseini*, 1977] where radiation efficiency is defined as the ratio of radiated energy to the sum of the radiated and fracture energy. Thus, from Figure 6, we can write $\eta_R = \dfrac{E_R}{E_R + E_G} = \dfrac{E_R}{(\sigma_0 - \sigma_1)\overline{D}S/2}$, where E_R is the radiated energy, and E_G is the fracture energy. Thus from the static stress drop, $\Delta\sigma_s = \sigma_0 - \sigma_1$, the radiated energy, E_R, and seismic moment, M_0, we can determine radiation efficiency

$$\eta_R = \frac{E_R}{E_R + E_G} = \frac{2\mu\tilde{e}}{\Delta\sigma_s}, \tag{1}$$

where $\tilde{e} = \frac{E_R}{M_0}$. Fracture energy is a part of the energy dissipated near the fault zone, and can be directly related to physical processes near the fault zone. *Husseini* [1977] used

Figure 4. Teleseismic energy estimates for six events (one event of each type) obtained using the single-station method are shown here. The event origin time (in yy-mm-dd format) and event name identifies the event (see Table 1 for other parameters). The first subplot for each earthquake shows the energy estimates at each of the teleseismic stations where the stations are plotted in order of increasing RMS radiation pattern factor; the second subplot for each earthquake is a plot of the energy estimates as function of station azimuth to show the azimuthal distribution of stations used to calculate energy. The open diamonds are the energy estimates obtained by integration of the squared velocity records in the time domain (no attenuation correction), while the solid circles are the energy estimates obtained by integration in the frequency domain with an attenuation correction that is modified from *Der* [1998] (details given by *Venkataraman et al.* [2002]).

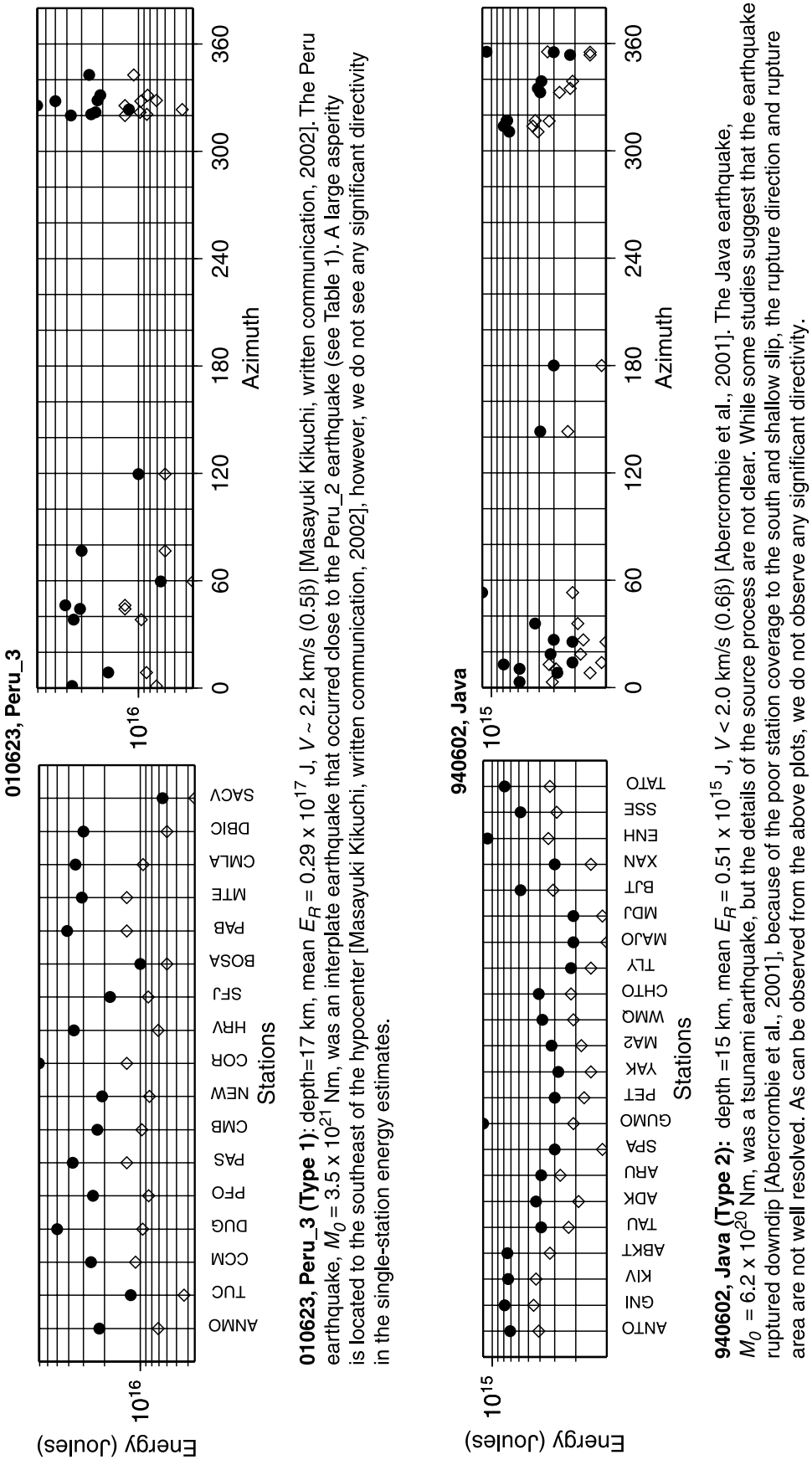

010623, Peru_3 (Type 1): depth=17 km, mean $E_R = 0.29 \times 10^{17}$ J, $V \sim 2.2$ km/s (0.5β) [Masayuki Kikuchi, written communication, 2002]. The Peru earthquake, $M_0 = 3.5 \times 10^{21}$ Nm, was an interplate earthquake that occurred close to the Peru_2 earthquake (see Table 1). A large asperity is located to the southeast of the hypocenter [Masayuki Kikuchi, written communication, 2002], however, we do not see any significant directivity in the single-station energy estimates.

940602, Java (Type 2): depth =15 km, mean $E_R = 0.51 \times 10^{15}$ J, $V < 2.0$ km/s (0.6β) [Abercrombie et al., 2001]. The Java earthquake, $M_0 = 6.2 \times 10^{20}$ Nm, was a tsunami earthquake, but the details of the source process are not clear. While some studies suggest that the earthquake ruptured downdip [Abercrombie et al., 2001], because of the poor station coverage to the south and shallow slip, the rupture direction and rupture area are not well resolved. As can be observed from the above plots, we do not observe any significant directivity.

Figure 4

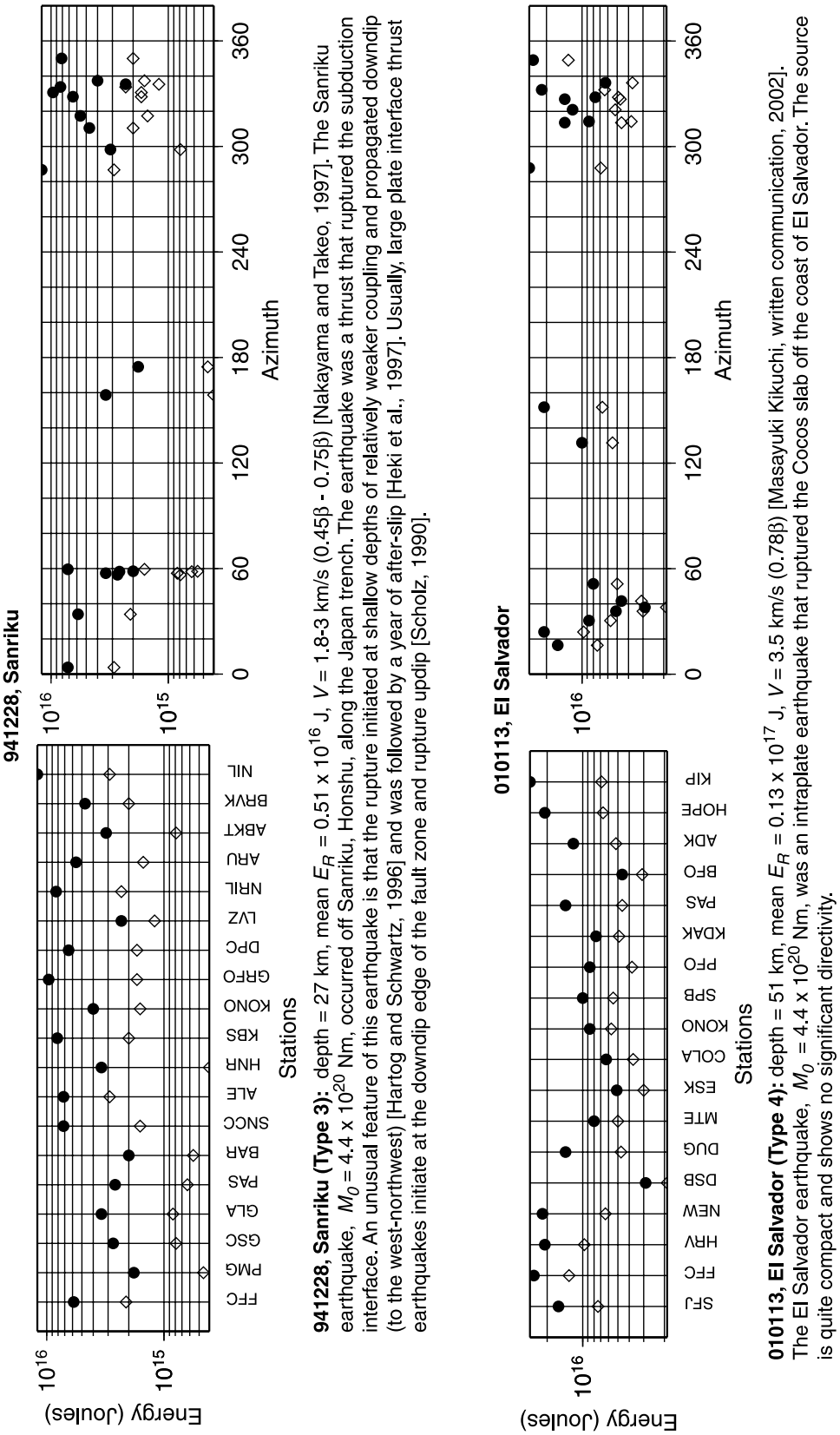

941228, Sanriku (Type 3): depth = 27 km, mean E_R = 0.51 x 10^{16} J, V = 1.8-3 km/s (0.45β - 0.75β) [Nakayama and Takeo, 1997]. The Sanriku earthquake, M_0 = 4.4 x 10^{20} Nm, occurred off Sanriku, Honshu, along the Japan trench. The earthquake was a thrust that ruptured the subduction interface. An unusual feature of this earthquake is that the rupture initiated at shallow depths of relatively weaker coupling and propagated downdip (to the west-northwest) [Hartog and Schwartz, 1996] and was followed by a year of after-slip [Heki et al., 1997]. Usually, large plate interface thrust earthquakes initiate at the downdip edge of the fault zone and rupture updip [Scholz, 1990].

010113, El Salvador (Type 4): depth = 51 km, mean E_R = 0.13 x 10^{17} J, V = 3.5 km/s (0.78β) [Masayuki Kikuchi, written communication, 2002]. The El Salvador earthquake, M_0 = 4.4 x 10^{20} Nm, was an intraplate earthquake that ruptured the Cocos slab off the coast of El Salvador. The source is quite compact and shows no significant directivity.

Figure 4. (continued)

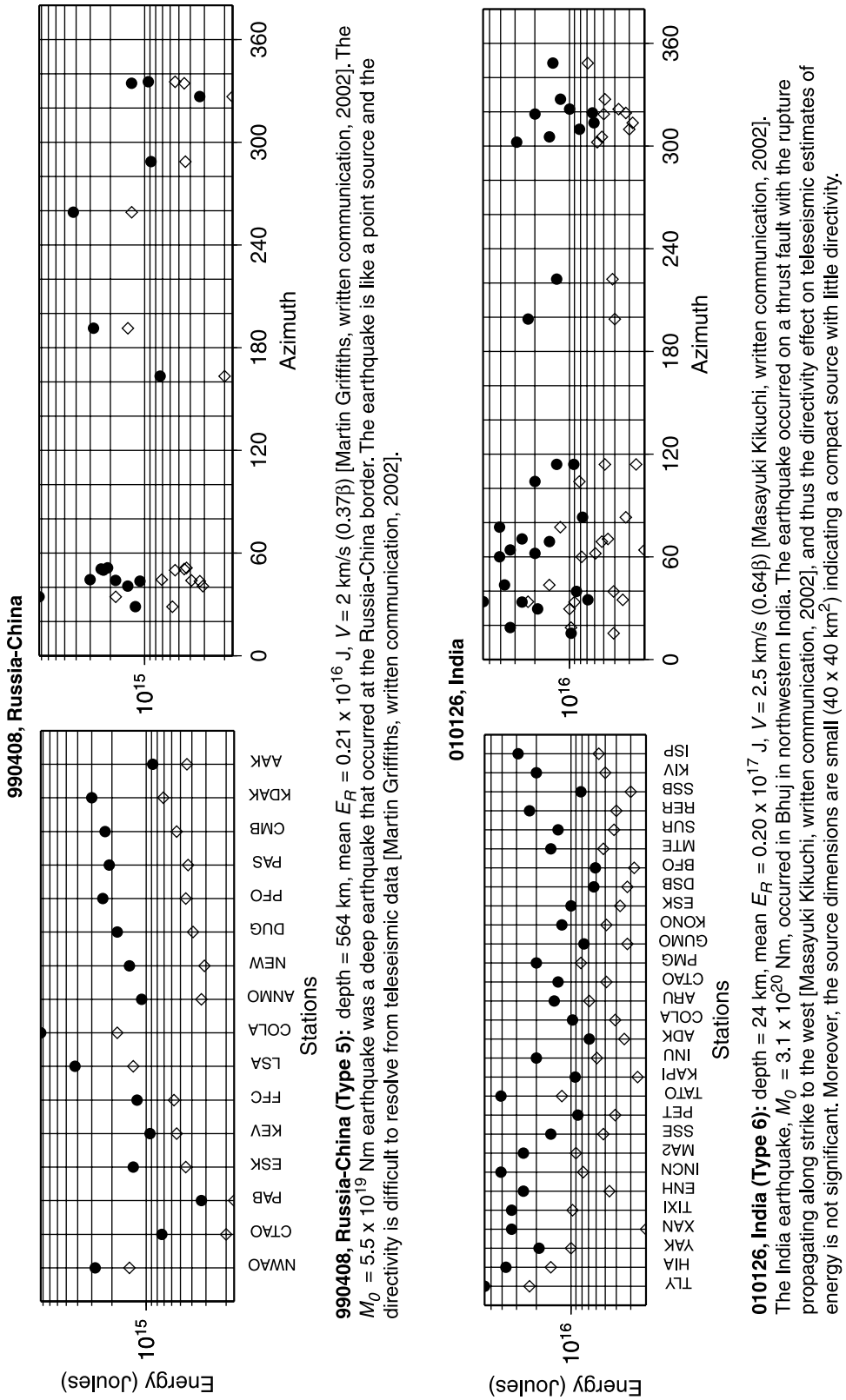

990408, Russia-China (Type 5): depth = 564 km, mean $E_R = 0.21 \times 10^{16}$ J, $V = 2$ km/s (0.37β) [Martin Griffiths, written communication, 2002]. The $M_0 = 5.5 \times 10^{19}$ Nm earthquake was a deep earthquake that occurred at the Russia-China border. The earthquake is like a point source and the directivity is difficult to resolve from teleseismic data [Martin Griffiths, written communication, 2002].

010126, India (Type 6): depth = 24 km, mean $E_R = 0.20 \times 10^{17}$ J, $V = 2.5$ km/s (0.64β) [Masayuki Kikuchi, written communication, 2002]. The India earthquake, $M_0 = 3.1 \times 10^{20}$ Nm, occurred in Bhuj in northwestern India. The earthquake occurred on a thrust fault with the rupture propagating along strike to the west [Masayuki Kikuchi, written communication, 2002], and thus the directivity effect on teleseismic estimates of energy is not significant. Moreover, the source dimensions are small (40 x 40 km^2) indicating a compact source with little directivity.

Figure 4. (continued)

Table 1. Radiated Energy Estimates of the Earthquakes Studied Here

Origin Time	Event Name	Latitude, deg	Longitude, deg	Depth, km	Dip, deg	Rake, deg	Strike, deg	Radiated Energy, Joules		Seismic Moment, Nm	Type[a]
								Mean	Median		
920902001557	Nicaragua	11.2°N	87.8°W	20	15°	91°	303°	0.43×10^{15}	0.47×10^{15}	3.1×10^{20}	2
930115110605	Kushiro-oki	43.1°N	144.3°E	107	11°	−30°	136°	0.43×10^{17}	0.26×10^{17}	3.1×10^{20}	4
930608130338	Kamchatka_1	51.4°N	158.8°E	46	29°	79°	207°	0.11×10^{16}	0.74×10^{15}	2.2×10^{20}	3
930712131736	Hokkaido	42.8°N	139.2°E	15	25°	104°	208°	0.18×10^{17}	0.16×10^{17}	5.5×10^{20}	1
940117123055	Northridge[b]	34.4°N	118.6°W	19	42°	116°	130°	0.13×10^{16}	NA	1.0×10^{19}	6
940309232807	Fiji-Tonga	17.7°S	178.1°W	569	27°	−30°	250°	0.20×10^{17}	0.17×10^{17}	2.8×10^{20}	5
940602181737	Java	11.0°S	113.0°E	15	83°	90°	99°	0.51×10^{15}	0.39×10^{15}	6.2×10^{20}	2
940609003345	Bolivia	13.8°S	67.5°W	647	89°	−103°	95°	0.13×10^{18}	0.88×10^{17}	2.9×10^{21}	5
941004132328	Shikotan	43.5°N	147.4°E	56	75°	125°	49°	0.15×10^{18}	0.95×10^{17}	2.6×10^{21}	4
941228121924	Sanriku	40.5°N	143.0°E	27	12°	67°	179°	0.51×10^{16}	0.44×10^{16}	4.4×10^{20}	3
950730051123	Chile	24.2°S	70.7°W	32	19°	110°	8°	0.26×10^{17}	0.22×10^{17}	1.8×10^{21}	1
951009153556	Jalisco	19.3°N	104.8°W	15	9°	92°	302°	0.82×10^{16}	0.41×10^{16}	1.2×10^{21}	1
951203180108	Kurile	44.8°N	150.2°E	26	12°	95°	225°	0.49×10^{16}	0.45×10^{16}	8.8×10^{20}	1
960221125104	Peru_1	9.9°S	80.2°W	15	21°	66°	330°	0.55×10^{15}	0.57×10^{15}	2.2×10^{20}	2
960610040335	Aleutian	51.1°N	177.4°W	29	17°	84°	248°	0.11×10^{17}	0.60×10^{16}	8.8×10^{20}	1
960617112216	Flores	7.4°S	123.0°E	588	55°	−51°	100°	0.62×10^{17}	0.33×10^{17}	7.3×10^{20}	5
961112165944	Peru_2	15.0°S	75.4°W	25	64°	110°	172°	0.10×10^{17}	0.90×10^{16}	3.5×10^{20}	1
970421120225	Santa-Cruz-Is	13.2°S	166.2°E	30	27°	35°	302°	0.19×10^{17}	0.16×10^{17}	5.7×10^{20}	1
971205112704	Kamchatka_2	54.3°N	161.9°E	34	23°	74°	202°	0.33×10^{16}	0.24×10^{16}	6.2×10^{20}	3
990408131034	Russia-China	43.6°N	130.3°E	564	28°	160°	81°	0.21×10^{16}	0.14×10^{16}	5.5×10^{19}	5
990817000139	Izmit	41.0°N	29.9°E	15	83°	181°	270°	0.14×10^{17}	0.11×10^{17}	3.1×10^{20}	6
990920174735	Chi-Chi	23.8°N	120.8°E	7	30°	85°	20°	0.88×10^{16}	0.64×10^{16}	3.1×10^{20}	6
991016094645	Hector[c]	34.5°N	116.3°W	7	78°	165°	330°	0.10×10^{16}	0.78×10^{15}	6.0×10^{19}	6
010113173331	El-Salvador	12.9°N	89.1°W	51	34°	−98°	119°	0.13×10^{17}	0.10×10^{17}	4.4×10^{20}	4
010126031641	India	23.5°N	70.3°E	24	50°	50°	65°	0.20×10^{17}	0.17×10^{17}	3.1×10^{20}	6
010228185436	Nisqually	47.0°N	122.5°W	52	71°	−99°	346°	0.96×10^{15}	0.78×10^{15}	1.9×10^{19}	4
010324062752	Geiyo	34.1°N	132.6°E	50	38°	−121°	323°	0.12×10^{16}	0.36×10^{15}	1.9×10^{19}	4
010623203313	Peru_3	16.1°S	73.3°W	17	16°	40°	301°	0.29×10^{17}	0.29×10^{17}	3.5×10^{21}	1

[a]Type 1, interplate earthquakes; Type 2, tsunami earthquakes; Type 3, downdip earthquakes; Type 4, intraplate earthquakes; Type 5, deep earthquakes; Type 6, crustal earthquakes.

[b]The radiated energy for the January 17, 1994, Northridge earthquake is the regional estimate used by *Kanamori and Heaton* [2000]. This estimate is in close agreement with the value obtained by *McGarr and Fletcher* [2001], about 3 times larger than the NEIC teleseismic estimate, and is about one half of the estimate published by *Mayeda and Walter* [1996].

[c]These estimates have been corrected for directivity.

this formulation to determine radiation efficiency, but due to the poor data quality available at the time, robust estimates of radiated energy were not possible and η_R could not be determined accurately. To determine η_R we require estimates of static stress drop. In the following section, we discuss the difficulties in the estimation of static stress drops and list the best estimates of static stress drops that we compiled from literature.

4.2. Static Stress Drop

[14] Static stress drop is defined as the change in the average state of stress on a fault before and after rupture. We estimate the average stress drop by

$$\Delta\sigma_S = C\mu\frac{\overline{D}}{\tilde{L}}, \tag{2}$$

where $\overline{D}$ is the average slip on the fault, $\tilde{L}$ is a characteristic rupture dimension, C is a non-dimensional constant that depends on the shape of the rupture surface and on the type of faulting (orientation of the shear stress), and μ is the shear modulus. The strain is $\overline{D}/\tilde{L}$. For a circular rupture, $\tilde{L} = a$, the radius of rupture; for rupture propagating on a rectangular fault, L is the length of the rupture and w is the width of the rupture. *Boore and Dunbar* [1977] computed the constant C for different depths of burial and for a range of aspect ratios, L/w. Subsequently, *Parsons et al.* [1988] found some inconsistencies in the published results and concluded that for most practical cases, C varies between 1.0 and 2.5.

[15] The actual stress drop on a fault can be very heterogeneous because of variations in stress and strength distribution on the fault plane. Thus the actual slip distribution on the fault plane could vary spatially resulting in very high stress drops locally, as compared to the average value over the fault [*Madariaga*, 1979]. However, we are interested in the average stress drop on the fault, a macroscopic parameter, and studies suggest that estimates of average stress drops will not be significantly affected by heterogeneous slip distribution except when slip is concentrated at the edges of the fault [*Madariaga*, 1977, 1979]. *Rudnicki and Kanamori* [1981] show that even in the case of heterogeneous slip distribution on the fault plane, unless the ratio of asperity length to fault size is very small (i.e., many small patches of slip on a large fault), the estimates of stress drop are good to within a factor of 2. Numerical experiments also suggest that for rectangular faults if we know the average slip and approximate fault geometry given by some large asperities, we can estimate the average stress drop to within 20% of the actual stress drop even if the actual distribution of asperities is not well determined [*Das*, 1988].

[16] Several methods are used to estimate stress drops (a discussion of the different methods is given by *Kanamori* [1994]). In this study, we used stress drops that were mostly determined from seismic moment and rupture area. Although seismic moment can be accurately determined, the rupture area is not always determined well. If dense seismic network data or geodetic (e.g., GPS or InSAR) data are

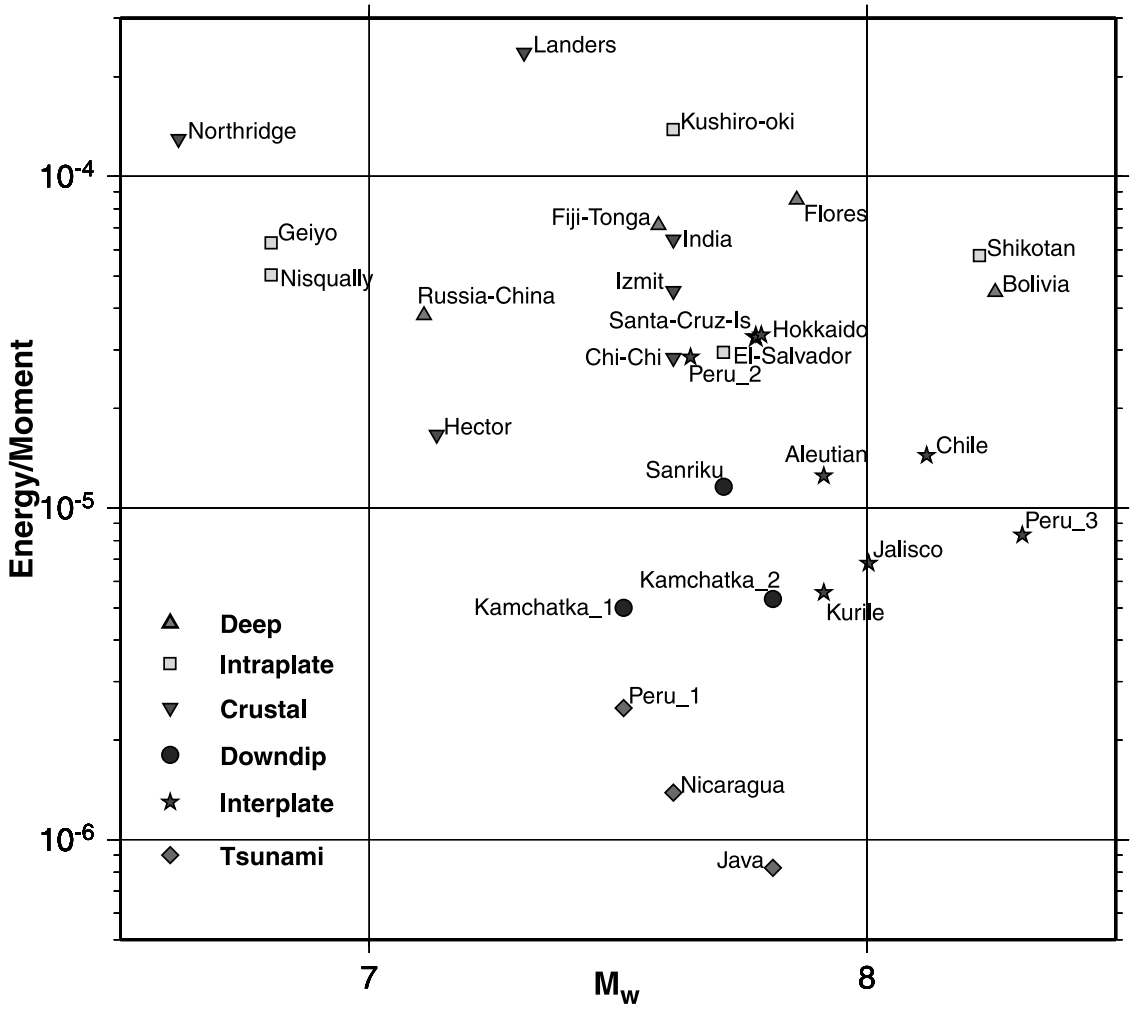

Figure 5. The computed energy-to-moment ratios plotted as a function of moment magnitude. The different symbols show different types of earthquakes as described in the legend. It is observed that tsunami earthquakes have the smallest energy-to-moment ratios, and crustal and deep earthquakes have the largest energy-to-moment ratios. See color version of this figure at back of this issue.

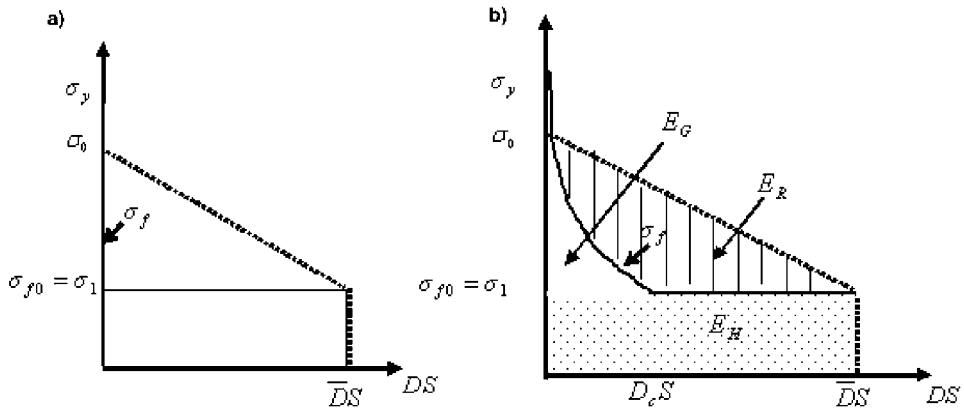

Figure 6. Schematic representation of the partitioning of energy in earthquakes. The plot shows stress as a function of slip times area. The dark line shows the variation of frictional stress, σ_f, on the fault as a function of slip. (a) The stress drops instantaneously from an initial to a final level. (b) In a physically realistic case, the stress first increases to the yield stress of the material, σ_y, and then drops to the final frictional stress level, σ_{f0}, over a critical slip, D_c. The fracture energy, E_G, dissipated in this process is shown by the unshaded region. The striped region represents the radiated energy, E_R, while the dotted region represents the heat energy, E_H, dissipated on the fault. Other symbols are explained in the text.

available near the source, the rupture area can be determined well. However, for many events, these data are not available, and the aftershock area or tsunami data are used to estimate the source dimension. For large events, the aftershock area generally coincides with the rupture area, but for moderate to small events, it is not necessarily representative of the co-seismic rupture area.

[17] Inversions for slip models generally use fault planes with dimensions exceeding the actual dimensions of the rupture area. In most slip models, heterogeneous slip distribution on the fault can result in regions on the fault that have almost zero slip and also the slip falls off toward the edges of the fault plane. Accordingly, these areas of low or zero slip have to be accounted for in determining an "effective" rupture area, i.e., the area where most of the slip is concentrated. Different investigators use different methods to tackle this issue; for example, *Somerville et al.* [1999] use a "trimming criteria." The seismic moment of the earthquake is slightly smaller after this trimming. *Mai and Beroza* [2000] on the other hand, use an autocorrelation width to determine the effective fault dimensions and also normalize the effective mean slip so that the seismic moment of the fault remains unchanged.

[18] For crustal earthquakes in California (Landers, Northridge, and Hector Mine), we use the rupture dimensions determined by *Nazareth* [2002], in which the trimming criteria of *Somerville et al.* [1999] are used. For example, to compute the static stress drop for the Hector Mine earthquake, if we use the formula for static stress drop, $\Delta\sigma_S = \frac{2}{\pi}\mu\frac{\overline{D}}{w}$, where $\overline{D}$ is the average slip on the fault, and w is the width, the average static stress drop over the three fault segments is 1.8 MPa for the rupture dimensions of the model of *Ji et al.* [2002], but if we use the trimmed rupture dimensions from *Nazareth* [2002] we obtain an average static stress drop of 3.2 MPa.

[19] A large number of static stress drop estimates listed in Table 2 were obtained from M. Kikuchi (written communication, 2002) in which the effective fault area is determined from slip models obtained by inversion of teleseismic data. The length over which most of the moment is concentrated is assumed to be the rupture length and the rupture width is assumed to be equal to half the rupture length. Even if the rupture length is 4 times the rupture width, the static stress drop estimates would differ by only a factor of 2. If M_0 is the seismic moment, and S is the rupture area, the stress drop, $\Delta\sigma_S$, can also be written as

$$\Delta\sigma_S = C\mu\frac{\overline{D}}{\tilde{L}} = C\frac{M_0}{S^{3/2}}.$$

In most of the estimates listed in Table 2, we used $C = 7\pi/16$, and in cases where the rupture broke the surface, a correction for the free-surface effect was included. As mentioned earlier, the stress drop estimates determined by different investigators could be different by a factor of two because of the different values of the constant, C used in the above formula. Moreover, determining the dimensions of the fault plane from inversion of teleseismic data is not very straightforward. It is difficult to determine the rupture area of shallow tsunami earthquakes because of the difficulty in modeling the lateral heterogeneities and complex structure close to the trench.

[20] For the 1994 Bolivia earthquake, which is the largest deep earthquake that has been well recorded, most investigators find that the rupture occurred over a small area with dimensions of about 40 km x 40 km or even smaller and hence the stress drops calculated using this dimension are very high (~110 MPa) [*Kikuchi and Kanamori*, 1994; *Goes and Ritsema*, 1995; *Antolik et al.*, 1996]. Because of the large size of the Bolivia earthquake, coupled with the fortuitous recording of the earthquake by an array of seismometers deployed almost on top of the epicenter, the rupture dimensions for this earthquake are probably better resolved than for other deep earthquakes. More generally, in case of deep earthquakes, unless the earthquake is large (like the Bolivia earthquake), the teleseismic signal-to-noise ratio is poor; moreover the source is almost like a point source for teleseismic waves. Thus it is difficult to determine the rupture length or rupture dimensions for small deep earthquakes unless a regional network is located close to the epicenter of the earthquake. We surveyed the available literature and for most earthquakes, we could obtain more than one estimate of the static stress drop. In some cases, we used some subjective judgement to decide on the representative rupture area. Table 2 is a compilation of the available stress drop estimates of the earthquakes studied here. Figure 7 shows the static stress drop estimates listed in Table 2 as a function of depth.

4.3. Radiation Efficiency

[21] Using the estimates of radiated energy, seismic moment and static stress drop, we calculated the radiation efficiency for all the earthquakes studied. Figure 8 is a plot of the radiation efficiencies as a function of moment magnitude for these earthquakes. From the figure, we observe that the radiation efficiency of most earthquakes lies between 0.25 and 1 (for explanation of radiation efficiency larger than 1, see Appendix B). Tsunami earthquakes, however, have small radiation efficiencies (<0.25) and the two deep earthquakes: the 1999 Russia-China border event and the 1994 deep Bolivia earthquake have small radiation efficiencies.

[22] From Figure 5, we observe that the ratio of radiated energy-to-moment is large for intraplate and deep earthquakes and for most crustal earthquakes, but from Figure 7 we observe that stress drop is also large for these earthquakes. This implies that the energy available for fracture and for the generation of seismic waves (as given by the top triangle in Figure 6b) is larger in these earthquakes. Similarly, the interplate and downdip extensional events have smaller energy-to-moment ratios, but the associated stress drops are also small. Hence, despite the differences in the radiated energy-to-moment ratios, because of the corresponding differences in static stress drops, interplate, downdip, intraplate and two deep earthquakes (Fiji-Tonga and Flores Sea earthquakes) have similar radiation efficiencies. Thus most earthquakes, except for tsunami earthquakes and the two deep earthquakes mentioned earlier, have radiation efficiencies between 0.25 and 1. *Kikuchi* [1992] performed a similar study, but concluded that most earthquakes have small radiation efficiencies. It is possible that the deficiency of high frequency energy in the slip models used by *Kikuchi*

Table 2. Static Stress Drop Estimates and Rupture Velocities of the Earthquakes Studied Here

	Stress Drop, MPa				Rupture Velocity, km/s			
Origin Time	Upper Limit	Lower Limit	Reference for Upper Limit	Reference for Lower Limit	Upper Limit	Lower Limit	Reference for Upper Limit	Reference for Lower Limit
920628115734 Landers (depth = 7 km)	5.5	2.6	Calculated from *Thio and Kanamori* [1996], using $\Delta\sigma_S = \frac{2}{\pi}\mu\frac{\overline{D}}{w}$ $\overline{D}$ = 3.5 m, w = 12 km	Calculated from *Nazareth* [2002], using $\Delta\sigma_S = \frac{2}{\pi}\mu\frac{\overline{D}}{w}$ $M_0 = 7.68 \times 10^{19}$ Nm, w = 15 km, L = 84 km	2.9	N.A.	*Dreger* [1994]	
920902001557 Nicaragua (depth = 20 km)	7.0	1.1	*Ihmle* [1996]	*Kanamori and Kikuchi* [1993]	1.0	1.5	*Ihmle* [1996]	*Kikuchi and Kanamori* [1995b]
930115110605 Kushiro-oki (depth = 107 km)	42.0	32.0	*Takeo et al.* [1993]	*Yoshiaka and Tokunaga* [1998]	3.3	N.A.	*Takeo et al.* [1993]	
930608130338 Kamchatka_1 (depth = 46 km)	1.6	NA	*Johnson et al.* [1995]		3.0	N.A.	*Johnson et al.* [1995]	
930712131736 Hokkaido (depth = 15 km)	4.0	NA	*Tanioka et al.* [1995]		3.0	N.A.	*Mendoza and Fukuyama* [1996]	
940117123055 Northridge (depth = 19 km)	4.6	3.2	Calculated from *Nazareth* [2002], (N-DR model) using $\Delta\sigma_S = \frac{7\pi^{3/2}}{16}\frac{M_0}{S^{3/2}}$ $M_0 = 1.05 \times 10^{19}$ Nm, $S = 14 \times 22$ km^2	Calculated from *Nazareth* [2002], (N-HV model) using $\Delta\sigma_S = \frac{7\pi^{3/2}}{16}\frac{M_0}{S^{3/2}}$ $M_0 = 1.63 \times 10^{19}$ Nm, $S = 20 \times 26$ km^2	2.7	3.0	*Zeng and Anderson* [1996]	*Wald et al.* [1996]
940309232807 Fiji-Tonga (depth = 569 km)	30.0	26.0	*Tibi et al.* [1999]	*Goes and Ritsema* [1995]	4.0	5.0	*Goes and Ritsema* [1995]	*Goes and Ritsema* [1995]; *Tibi et al.* [1999]
940602181737 Java (depth = 15 km)	1.0	0.3	Calculated from *Tanioka and Satake* [1996], using $\Delta\sigma_S = \frac{1}{2}\frac{7\pi^{3/2}}{16}\frac{M_0}{S^{3/2}}$ $M_0 = 3.5 \times 10^{20}$ Nm, $S = 90 \times 60$ km^2	*Abercrombie et al.* [2001]	2.0	N.A.	*Abercrombie et al.* [2001]	
940609003345 Bolivia (depth = 647 km)	280.0	110.0	*Goes and Ritsema* [1995]	*Kikuchi and Kanamori* [1994]	1.0	2.0	*Kikuchi and Kanamori* [1994]	*Goes and Ritsema* [1995]
941004132328 Shikotan (depth = 56 km)	14.0	11.0	*Ozawa* [1996]	*Kikuchi and Kanamori* [1995a]	2.5	N.A.	*Kikuchi and Kanamori* [1995a, 1995b]	
941228121924 Sanriku (depth = 27 km)	3.1	2.6	*Sato et al.* [1996]	Kikuchi's web site[a]	1.8	3.0	*Nakayama and Takeo* [1997]	*Nakayama and Takeo* [1997]
950730051123 Chile (depth = 32 km)	3.3	1.6	Calculated from Kikuchi's web site using $\Delta\sigma_S = \frac{1}{2}\frac{7\pi^{3/2}}{16}\frac{M_0}{S^{3/2}}$ $M_0 = 1.7 \times 10^{21}$ Nm, $S = 120 \times 60$ km^2	Calculated from *Carlo et al.* [1999], using $\Delta\sigma_S = \frac{1}{2}\frac{7\pi^{3/2}}{16}\frac{M_0}{S^{3/2}}$ $M_0 = 1.6 \times 10^{21}$ Nm, $S = 190 \times 60$ km^2	3.3	N.A.	*Reugg et al.* [1996]	
951009153556 Jalisco (depth = 15 km)	1.6	0.4	Calculated from *Pacheco et al.* [1997], using $\Delta\sigma_S = \frac{1}{2}\frac{7\pi^{3/2}}{16}\frac{M_0}{S^{3/2}}$ $M_0 = 1.8 \times 10^{21}$ Nm, $S = 170 \times 70$ km^2	Calculated from *Mendoza and Hartzell* [1999], using $\Delta\sigma_S = \frac{1}{2}\frac{7\pi^{3/2}}{16}\frac{M_0}{S^{3/2}}$ $M_0 = 8.3 \times 10^{20}$ Nm, $S = 200 \times 100$ km^2	2.2	2.8	*Escobedo et al.* [1998]	*Courboulex et al.* [1997]

Table 2. (continued)

Origin Time	Stress Drop, MPa				Rupture Velocity, km/s			
	Upper Limit	Lower Limit	Reference for Upper Limit	Reference for Lower Limit	Upper Limit	Lower Limit	Reference for Upper Limit	Reference for Lower Limit
951203180108 Kurile (depth = 26 km)	3.5	1.5	Kikuchi's web site	Calculated from *Hurukawa* [1998], using $\Delta\sigma_S = \frac{7\pi^{3/2}}{16}\frac{M_0}{S^{3/2}}$ $M_0 = 8.8 \times 10^{20}$ Nm, $S = 140 \times 90$ km^2	2.5	N.A.	*Schwartz* [1999]	
960221125104 Peru_1 (depth = 15 km)	4.9	0.8	Kikuchi's web site	Calculated from *Ihmle et al.* [1998], using $\Delta\sigma_S = \frac{1}{2}\frac{7\pi^{3/2}}{16}\frac{M_0}{S^{3/2}}$ $M_0 = 2.0 \times 10^{20}$ Nm, $S = 110 \times 40$ km^2	1.5	2.0	*Ihmle et al.* [1998]	*Ihmle et al.* [1998]
960610040335 Aleutian (depth = 29 km)	4.1	2.9	Calculated from *Tanioka and Gonzalez* [1998], using $\Delta\sigma_S = \frac{1}{2}\frac{7\pi^{3/2}}{16}\frac{M_0}{S^{3/2}}$ $M_0 = 7.3 \times 10^{20}$ Nm, $S = 120 \times 30$ km^2	Kikuchi's web site	2.2	N.A.	Calculated from Kikuchi's web site	Kikuchi's web site
960617112216 Flores (depth = 588 km)	30.0	16.0	*Tibi et al.* [1999]	*Goes et al.* [1997]	2.0	4.0	*Goes et al.* [1997]	*Tibi et al.* [1999]
961112165944 Peru_2 (depth = 25 km)	3.7	3.0	Calculated from *Swenson and Bilek* [1999], using $\Delta\sigma_S = \frac{7\pi^{3/2}}{16}\frac{M_0}{S^{3/2}}$ $M_0 = 3.4 \times 10^{20}$ Nm, $S = 90 \times 45$ km^2	Kikuchi's web site	2.25	N.A.	*Swenson and Bilek* [1999]	
970421120225 Santa-Cruz-Is (depth = 30 km)	4.0	2.2	*Kaverina et al.* [1998]	Kikuchi's web site	1.9	N.A.	*Kaverina et al.* [1998]	
971205112704 Kamchatka_2 (depth = 34 km)	2.7	2.5	Kikuchi's web site	Calculated from *Wha* [1998], using $\Delta\sigma_S = \frac{7\pi^{3/2}}{16}\frac{M_0}{S^{3/2}}$ $M_0 = 2.5 \times 10^{20}$ Nm, $S = 88 \times 44$ km^2	2.0	N.A.	*Wha* [1998]	
990408131034 Russia-China (depth = 564 km)	16.0	NA	Martin Griffith, written communication, 2002		2.0	N.A.	Martin Griffith, written communication, 2002	
990817000139 Izmit (depth = 15 km)	12.0	9.1	*Tibi et al.* [2001]	Kikuchi's web site	3.0	N.A.	*Yagi and Kikuchi* [2000]	
990920174735 Chi-Chi (depth = 7 km)	3.2	2.1	Kikuchi's web site	Calculated from *Ji et al.* [2003], using $\Delta\sigma_S = \frac{1}{2}\frac{7\pi^{3/2}}{16}\frac{M_0}{S^{3/2}}$ $M_0 = 2.7 \times 10^{20}$ Nm, $S = 2924$ km^2	2.0	N.A.	*Ji et al.* [2003]	

Table 2. (continued)

Origin Time	Stress Drop, MPa				Rupture Velocity, km/s			
	Upper Limit	Lower Limit	Reference for Upper Limit	Reference for Lower Limit	Upper Limit	Lower Limit	Reference for Upper Limit	Reference for Lower Limit
991016094645 Hector (depth = 7 km)	3.2	1.4	Calculated from *Nazareth* [2002] (H-J model) method discussed in text	Calculated from *Nazareth* [2002] (H-K model) method discussed in text	1.9	N.A.	*Ji et al.* [2002]	
010113173331 El-Salvador (depth = 51 km)	13.0	NA	Kikuchi's web site		3.5	N.A.	Calculated from Kikuchi's web site	
010126031641 India (depth = 24 km)	24.6	12.6	*Negishi et al.* [2002]	*Negishi et al.* [2002]	2.5	N.A.	*Negishi et al.* [2002]	
010228185436 Nisqually (depth = 52 km)	23.0	NA	Kikuchi's web site		2.5	N.A.	Calculated from Kikuchi's web site	
010324062752 Geiyo (depth = 50 km)	13.0	NA	Kikuchi's web site		2.9	N.A.	Calculated from Kikuchi's web site	
010623203313 Peru_3 (depth = 17 km)	1.4	NA	Kikuchi's web site		2.2	N.A.	Calculated from Kikuchi's web site	

[a]M. Kikuchi's web site from M. Kikuchi (written communication, 10 April 2002). For events from 1991 to June 1996, data available at http://wwweic.eri.u-tokyo.ac.jp/EIC/YCU_report/. For events from August 1996 to March 2002, data available at http://wwweic.eri.u-tokyo.ac.jp/EIC/EIC_News/index.html.

[1992] to compute radiated energy resulted in low values of the energy to moment ratios.

4.4. Radiation Efficiency and Rupture Velocity

[23] Radiation efficiency, η_R, can be estimated independently from rupture velocity, V. The ratio of rupture velocity and limiting rupture speed (V/c_L) can be related to radiation efficiency by

$$\eta_R = \frac{E_R}{E_R + E_G} = 1 - g(V), \tag{3}$$

where $g(V)$ is a unique function of rupture speed V. For a Mode I (tensile) crack [*Freund*, 1972]

$$g(V) = 1 - V/c_R, \tag{4a}$$

for a Mode II (longitudinal shear) crack [*Fossum and Freund*, 1975]

$$g(V) = (1 - V/c_R)/\sqrt{1 - V/c_S}, \tag{4b}$$

and for Mode III (transverse shear) crack [*Kostrov*, 1966; *Eshelby*, 1969],

$$g(V) = \sqrt{\frac{1 - (V/c_S)}{1 + (V/c_S)}}, \tag{4c}$$

c_R is the Rayleigh wave speed and c_S is the shear wave speed.

[24] Also, from simple energy considerations [*Mott*, 1948; *Lawn*, 1993], the radiation efficiency can be expressed as

$$\eta_R = \frac{E_R}{E_R + E_G} = (V/c_L)^2.$$

From the above, we observe that the radiation efficiency is small for small V/c_L.

[25] Table 2 also includes a compilation of rupture velocities from literature for the earthquakes we studied. Average rupture velocities are usually determined from inversion of seismic waves and the results can be non-unique, but for most of the larger earthquakes, the estimates of rupture velocities are quite robust. Most of these earthquakes have rupture velocities such that the ratio of rupture velocity to shear wave speed (V/β) is between 0.6 and 0.85 and for these earthquakes the radiation efficiency is between 0.3 and 1. However, the 1994 Bolivia earthquake, the 1999 Russia-China border event and the tsunami earthquakes, have small V/β as well as small radiation efficiencies. Figure 9 shows the upper and lower limit of radiation efficiencies that were determined earlier plotted against the upper and lower limit of V/β obtained from literature (shown in Table 2). The theoretical curves relating radiation efficiency to rupture velocity for Mode I, Mode II and Mode III cracks have also been plotted on the same figure. The figure shows that, to the first order, the observed data follow the theoretical curves obtained from crack theory. Since rupture velocity is an independently determined quantity, this consistency in the observed relationship

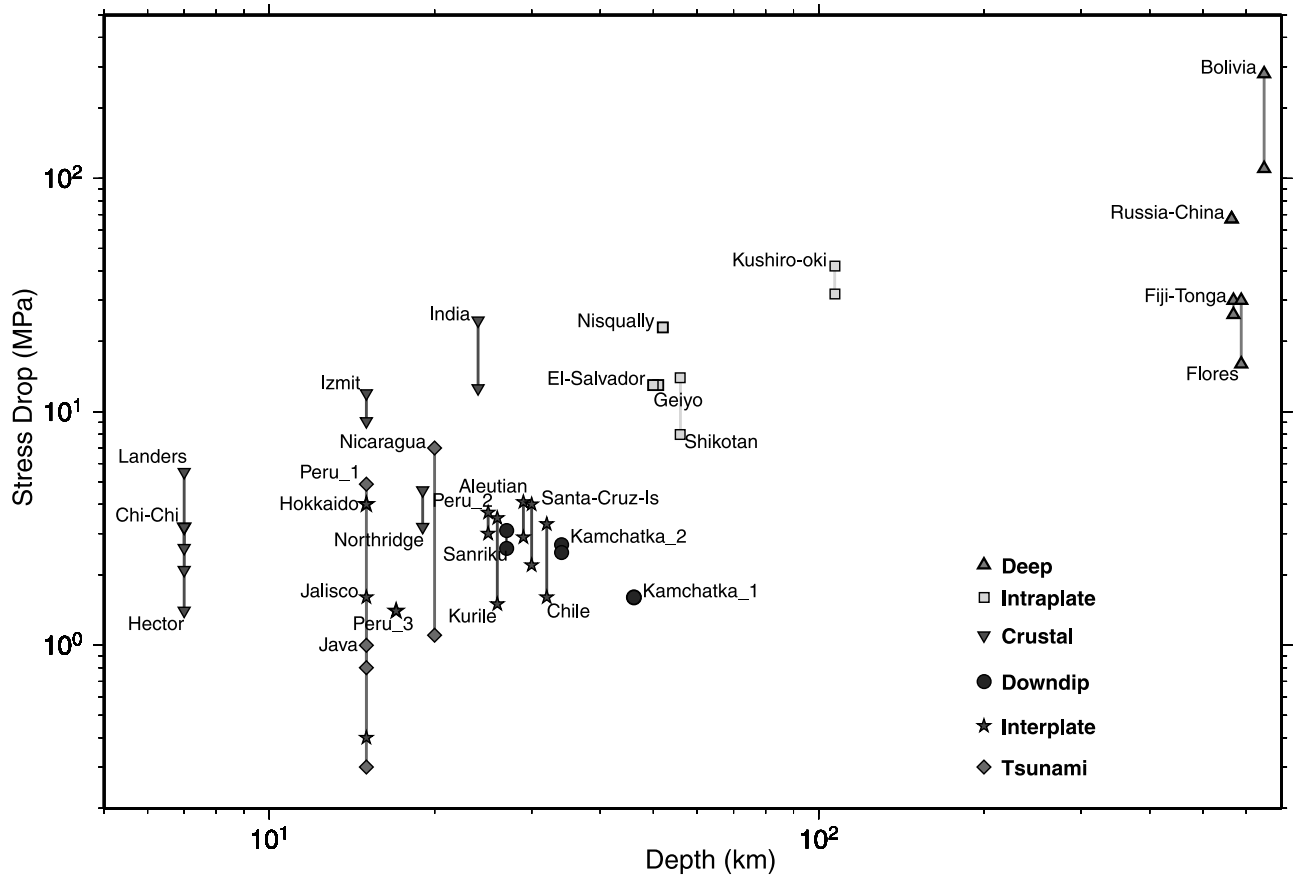

Figure 7. Static stress drop plotted as a function of depth for the different types of earthquakes studied. See color version of this figure at back of this issue.

between radiation efficiency and V/β on the one hand, and the calculations from crack theory on the other suggests that the use of the simple energy diagram shown in Figure 6b is appropriate for most earthquakes.

[26] Radiation efficiency can also be estimated from critical slip, D_C where, $\eta_R = 1 - D_C/D$. However, due to the low-pass filtering used in most modeling studies, the current estimates of D_C should be regarded as upper bound; thus only a lower limit of radiation efficiency can be determined [*Ide and Takeo*, 1997; *Olson et al.*, 1997; *Guatteri and Spudich*, 2000].

[27] The accuracy of the radiation efficiency, η_R estimated from equation (1) depends on the accuracy of the estimates of E_R, M_0, and $\Delta\sigma_S$. Although it is difficult to determine the real uncertainties in these parameters, the variation of these parameters determined for the same event by different investigators using different methods provides a common-sense estimate of the uncertainties as described by *Venkataraman and Kanamori* [2004].

[28] For the events studied here, the seismic moment, M_0, estimated by different investigators using different methods seldom varies by more than 30%. The estimates of E_R and $\Delta\sigma_S$ are more uncertain and mainly determine the uncertainties in η_R. It is not uncommon to see a factor of 2 variation in $\Delta\sigma_S$ and a factor of 3 variation in E_R for the same event in literature. In this study, we chose events for which these macroscopic parameters are constrained better than the average, and we estimate that $\Delta\sigma_S$ is uncertain by a factor of 1.5 (except for a few cases where larger ranges are observed), and E_R by a factor of 2. Then, $Var(\log E_R) \approx \log 2$ and $Var(\log \Delta\sigma_S) \approx \log 1.5$. Assuming a normal distribution of error, $Var(\log \eta_R) = [Var(\log E_R) + Var(\log \Delta\sigma_S)]^{1/2} \propto 0.349$, which implies that η_R is uncertain by a factor of $10^{0.349} = 2.2$. The above argument is qualitative, but provides some measure of uncertainty of the radiation efficiency we obtained. If we allow either more optimistic or more pessimistic uncertainties for $\Delta\sigma_S$ and E_R, the uncertainty of η_R varies accordingly.

[29] Although the values of η_R estimated from of E_R, M_0, and $\Delta\sigma_S$ are unfortunately fairly large, the overall consistency of these values with those independently estimated from the rupture speed (Figure 9) suggests that, even if the uncertainty in the estimate of η_R for an individual event may be considerably large, the overall trend shown in Figure 8 is robust.

5. Discussions

[30] In the following section, we discuss possible explanations for the small radiation efficiencies of deep earthquakes and tsunami earthquakes.

5.1. Deep Earthquakes

[31] The 1994, Bolivia earthquake is the largest deep focus earthquake that has been instrumentally recorded [*Kikuchi and Kanamori*, 1994]. Studies have shown that the rupture propagated very slowly (~1 km/s) in this earthquake [*Kikuchi and Kanamori*, 1994; *Silver et al.*,

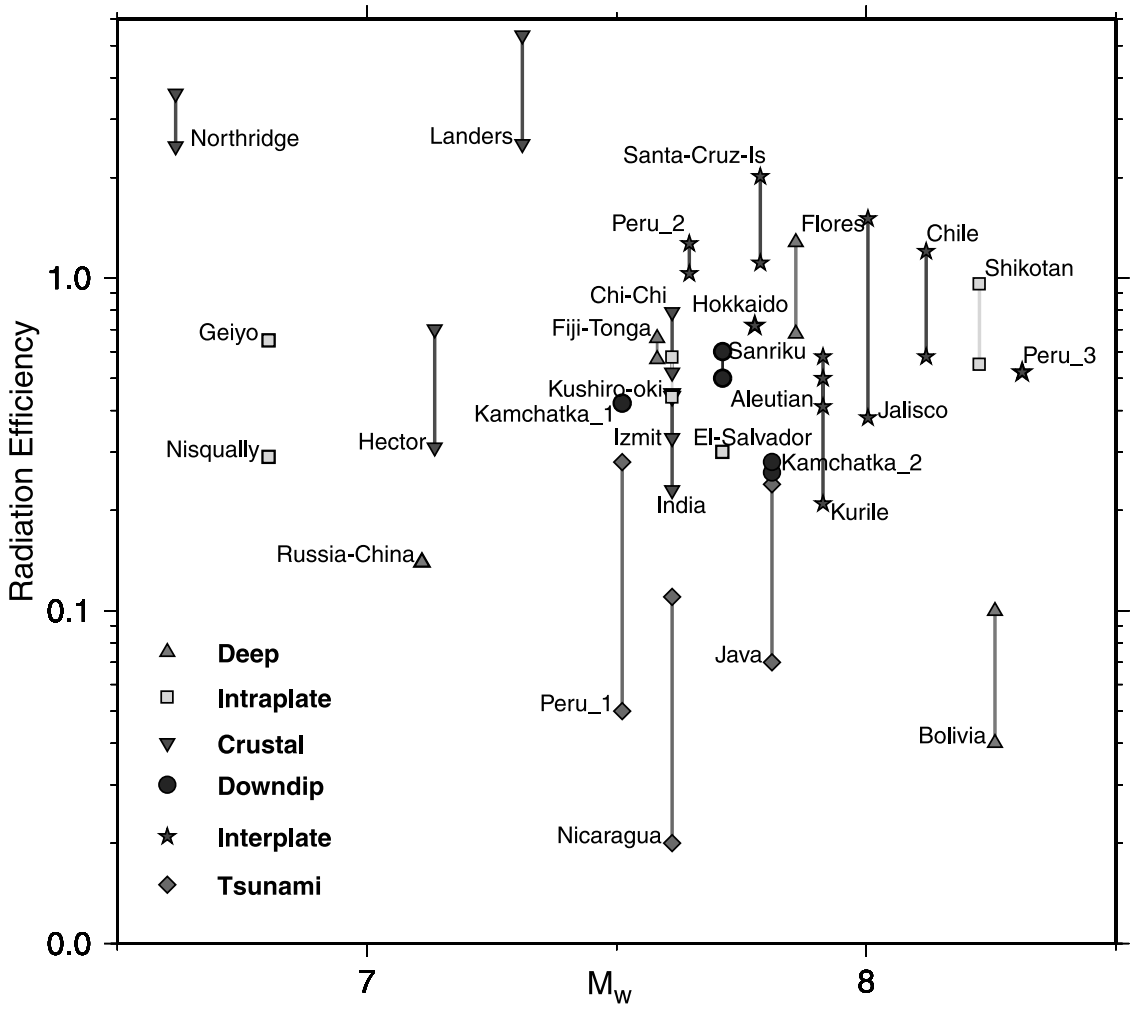

Figure 8. Radiation efficiencies determined from the radiated energy-to-moment ratios are plotted as a function of moment magnitude. The different symbols show different types of earthquakes as described in the legend. Most earthquakes have radiation efficiencies greater than 0.25, but tsunami earthquakes and two of the deep earthquakes (the Bolivia earthquake and the Russia-China earthquake) have small radiation efficiencies. See color version of this figure at back of this issue.

1995] and the earthquake had a very large static stress drop (110 MPa–280 MPa) [*Kikuchi and Kanamori*, 1994; *Goes and Ritsema*, 1995]. *Kanamori et al.* [1998] proposed that the earthquake involved large energy dissipation during faulting which resulted in frictional melting. In this study, we observe that the radiation efficiency of this event is very small (between 0.1 and 0.04) indicating that a large amount of energy of about 1×10^{18} J to 3×10^{18} J was dissipated. Earlier studies [*Kikuchi*, 1992; *Kanamori et al.*, 1998; *Wiens*, 2001] assume that the dissipated energy was completely used in frictional heating. However, within the framework of the energy diagram shown in Figure 6b, the dissipated energy is equal to the fracture energy, but the partition of dissipated energy into fracture energy and heat energy depends on the details of the process; it is possible that a significant fraction of this dissipated energy was eventually transformed to heat in the fault zone.

[32] The 1999 Russia-China border earthquake also has small radiation efficiency (about 0.14); the average rupture velocity for this event is small, about 2 km/s (M. Griffiths, written communication, 2002). *Tibi et al.* [2003] determined the rupture velocity of this earthquake to be 2.5 km/s and low radiation efficiency (0.073). The 1994 Bolivia earthquake and the 1999 Russia-China border earthquake are unlike the other two deep earthquakes studied; the 1994 Fiji-Tonga earthquake and the 1996 Flores Sea earthquake have radiation efficiencies larger than 0.5, much smaller static stress drops and rupture velocities between 3–5 km/s (V/β between 0.7 and 0.9) [*Goes and Ritsema*, 1995; *Tibi et al.*, 1999].

[33] The Fiji-Tonga slab and the slab that subducts beneath the Flores Sea region have a large number of small deep earthquakes, i.e., large b-values, while the South American slab and the Japan slab that ruptured in the Russia-China border earthquake have small b-values [*Giardini*, 1988; *Frolich*, 1989; *Wiens and Gilbert*, 1996; *Wu and Chen*, 2001]. *Wiens and Gilbert* [1996] and *Wiens* [2001] use a thermal parameter which is defined as the product of the slab vertical descent rate and the age of the subducting lithosphere as a measure of the temperature of the slab at depth; a larger thermal parameter is indicative of a colder slab at depth. They observe a systematic relation-

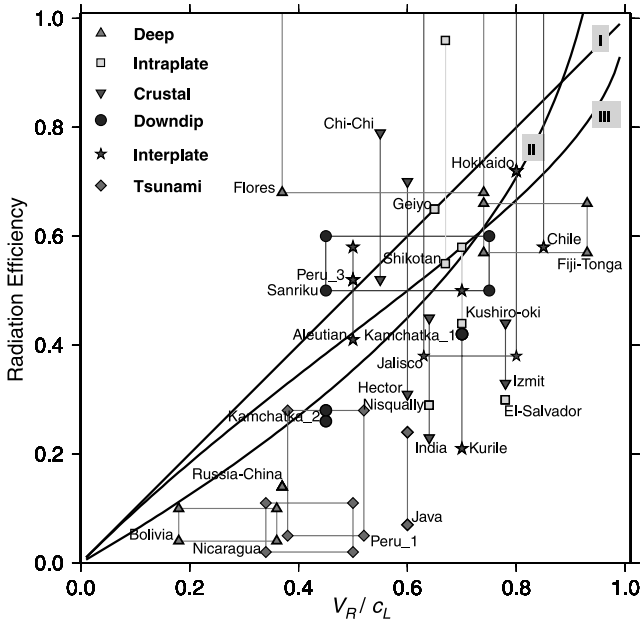

Figure 9. Radiation efficiencies determined from the radiated energy-to-moment ratios and estimates of static stress drop plotted against the estimates of the ratio of rupture velocity to shear wave velocity obtained from literature. Symbols are the same as before; for comparison, the theoretical curves relating radiation efficiency to rupture velocity for Mode I, Mode II, and Mode III cracks have also been plotted. See color version of this figure at back of this issue.

ship between b-values and the thermal parameter in slabs—slabs with smaller b-values have smaller thermal parameter and are hence warmer. Further, they also observe that the radiation efficiency (they call it seismic efficiency) increases with an increase in thermal parameter. Thus our results are consistent with their observations—the 1994 Bolivia earthquake has the smallest radiation efficiency and correspondingly the smallest thermal parameter, both parameters are slightly larger for the 1999 Russia-China event that occurred in the Japan slab, and even larger for the 1996 Flores Sea and the 1994 Fiji-Tonga events.

[34] Several mechanisms have been proposed for deep earthquake faulting [*Meade and Jeanloz*, 1991; *Green and Burnley*, 1989; *Karato et al.*, 2001; *Kirby et al.*, 1991]. There have been several attempts to use seismological parameters to constrain the faulting mechanism [*Frolich*, 1989; *Green and Houston*, 1995] and the more recent studies [*Wiens*, 2001; *Karato et al.*, 2001] favor creep induced shear instabilities as the probable mechanism for deep earthquake faulting. *Wiens* [2001] and *Karato et al.* [2001] argue that thermal shear instabilities would be able to explain most seismological observations. In creep induced thermal instabilities, temperature in a zone increases due to shear heating, but due to viscous dissipation, the width of this zone decreases gradually. However, at a critical width of the shear zone, the temperature increases explosively and the stress drops rapidly; this causes melting and thus induces slip in the shear zone, i.e., an earthquake [*Griggs and Baker*, 1968; *Ogawa*, 1990]. Since large deep earthquakes (e.g., the Bolivia earthquake) involve coseismic melting along narrow zones [*Kanamori et al.*, 1998] thermal instability is a plausible mechanism for these earthquakes.

[35] Why do warmer slabs favor stress release through large earthquakes with high stress drops while colder slabs favor stress release through small earthquakes with smaller stress drops? According to the thermal runaway model [*Karato et al.*, 2001], colder slabs have higher strain rates (larger deformation) and hence will result in a large number of earthquakes (as observed in the Fiji-Tonga region). Though warmer slabs have smaller strain rates, once a sufficient amount of strain has been accumulated, a thermal instability can be initiated, and because of the higher temperature, once the instability is initiated it can cascade into a large earthquake. This would explain the infrequent large earthquakes in warm slabs. Moreover, since the temperature in warmer slabs is higher, the rupture mechanism would involve a large amount of melt and hence the growth of the fault would be a very dissipative process. However, thermal instability models depend strongly on the effects of temperature on slab rheology and these effects are not yet well understood. Such ''creep rupture'' [*Lawn*, 1993] is a vast area of study and further work is required to understand it better.

5.2. Tsunami Earthquakes

[36] From Figure 8, we observe that tsunami earthquakes have small radiation efficiencies. Thus these earthquakes dissipate a large amount of energy during the fracture process and are left with little energy to radiate. Tsunami earthquakes are also known to have small rupture velocities and hence involve slow rupture [*Kanamori*, 1972; *Kanamori and Kikuchi*, 1993; *Polet and Kanamori*, 2000]. These earthquakes rupture the shallow portions of subduction zones resulting in a large amount of slip occurring very close to the ocean surface. To the first order, the size of a tsunami is proportional to the amount of water displaced at the tsunami source, which is proportional to the volume of the displaced ocean surface [*Kajiura*, 1970; *Kanamori*, 1972]; thus the large amount of fault slip close to the ocean floor causes more displacement of the ocean floor and generates larger tsunamis than would be expected if the same amount of slip had occurred deeper. *Tanioka and Satake* [1996] and *Polet and Kanamori* [2000] also suggest that since the near surface structure plays a critical role in estimating the distribution of fault slip in tsunami events, the actual displacement on the ocean floor calculated from the seismic moment may be underestimated due to the presence of lateral heterogeneities that are usually not accounted for in seismic source inversions.

[37] Most tsunami earthquakes rupture updip toward the trench in regions where the ocean floor close to the trench is highly faulted, has a small accretionary prism and a thin veneer of sediments [*Tanioka et al.*, 1997; *Polet and Kanamori*, 2000]. The presence of sediments has been used to explain the slow character of these tsunami events. Our results suggest high fracture energy in tsunami earthquakes. It is probable that the highly faulted trench and deformed sediments results in larger energy dissipation during failure. It has been observed that highly damaged material has an excessive amount of branching and bifurcation of cracks which gives rise to inelastic behavior and hence a large dissipation of energy [*Barragan et al.*, 2001]. Similarly, it is

possible that the morphology of the trench causes branching and bifurcation of rupture, resulting in the large energy dissipation during the rupture process of tsunami earthquakes.

5.3. Specific Fracture Energy

[38] As shown above, the fracture energy, E_G can be determined from seismic moment, radiated energy and static stress drop using equation (1), or from rupture velocity using equation (4). With these two independent methods, we showed that the fracture energy for most large events is, at most, comparable to E_R. Since $E_G + E_R = (1/2)\Delta\sigma_S DS$ from Figure 6b, this means that $E_G \leq (1/4)\Delta\sigma_S DS$. Thus the specific surface energy, $G = E_G/S$ is at most of the order of $G = E_G/S \leq (1/4)D\Delta\sigma_S$. Assuming D = 3 m, and $\Delta\sigma_S$ = 30 bar, G can be as large as 2 MJ/m^2, which is the value often quoted in seismology [*Rice*, 1980; *Li*, 1987; *Scholz*, 1990]. This value is much larger than that directly measured for crystals and metals, 1 to 100 J/m^2, and should not be interpreted as the specific surface energy in the ordinary sense. It should be interpreted as energy dissipated in a finite volume near the crack tip, in the breakdown zone, or outside of the main fault surface. The surface energy increases with rupture speed, V, as a result of surface roughening due to multiple fractures or extensive plastic deformation near the crack tip, as has been experimentally demonstrated by *Ravichandar and Knauss* [1984], and *Rosakis and Zehnder* [1985], respectively. Also, *Poliakov et al.* [2002] suggest that a part of the fracture energy is dissipated outside the main fault surface where secondary failure occurs in the damage zone. *Janssen et al.* [2001], calculate the fracture energy involved in deformation of experimental samples using a formula: $G_f = 0.5G_G(\rho_C V_C + A_{mf})$, where G_f is the fracture energy, G_G is the specific fracture energy, ρ_C is the density of cracks and V_C is the volume of the fracture process zone (or breakdown zone) and A_{mf} is the fault area. Using a relationship like this would include the deformation in a volume around the crack tip.

[39] Thus it is probably more appropriate to interpret the fracture energy of earthquake as the energy which is mechanically dissipated in a finite volume near the damaged zone and outside of the main fault surface.

6. Conclusions

[40] For the earthquakes studied, we observe that the radiated energy-to-moment ratio is different for different types of earthquakes; tsunami earthquakes have the smallest radiated energy-to-moment ratio (7×10^{-7} to 3×10^{-6}), interplate and downdip earthquakes have a slightly larger ratio (5×10^{-6} to 2×10^{-5}) and intraplate and deep earthquakes have ratios similar to crustal earthquakes (2×10^{-5} to 3×10^{-4}). We computed radiation efficiencies for these earthquakes using the energy budget for a slip-weakening model, and observe that most earthquakes have large radiation efficiencies between 0.25 and 1, while tsunami earthquakes and some deep earthquakes like the 1994 Bolivia earthquake and the 1999 Russia-China border earthquake have small radiation efficiencies (<0.25) and hence dissipate a large amount of energy. In case of these deep events, the energy is probably dissipated in thermal processes, while it is possible that the morphology of the trench causes branching and bifurcation of rupture, resulting in the large energy dissipation during the rupture process of tsunami earthquakes.

Appendix A: Definition of Average Quantities

[41] In this study, we use macroscopic parameters to understand the mechanics of earthquake rupture. The macroscopic parameters used are the average of physical parameters over the fault plane as well as over the slip at a given location on the fault. Several assumptions are made in using these averages. The definitions of these parameters used in sections 4.1 and 4.2, are given in this section.

[42] 1. The total potential energy released in an earthquake is

$$\Delta W = \int_S D\frac{(\sigma_0 + \sigma_1)}{2} dS, \tag{A1}$$

where D is the slip on the fault plane, and σ_0 and σ_1 are the initial and final stresses on the fault plane, respectively. Here D, σ_0 and σ_1 are generally functions of position on the fault plane. The integration is over the fault area, S. We define the spatial averages of D, σ_0 and σ_1 by

$$\overline{D} = \frac{1}{S}\int_S DdS, \overline{\sigma}_0 = \frac{1}{S}\int_S \sigma_0 dS, \text{ and } \overline{\sigma}_1 = \frac{1}{S}\int_S \sigma_1 dS, \tag{A2}$$

respectively. Using these, we approximate ΔW by

$$\Delta W \approx \overline{D}\frac{(\overline{\sigma}_0 + \overline{\sigma}_1)}{2} S \equiv \overline{D}\overline{\sigma}S, \tag{A3}$$

where $\overline{\sigma}$ is the arithmetic average of σ_0 and σ_1 and is often called the average stress on the fault plane. In this paper we use equation (A3) for ΔW with the assumption that equation (A3) is a good macroscopic approximation of equation (A1).

[43] 2. The dissipated energy in an earthquake is given as (Figure 6b)

$$E_G + E_H = \int_S \overline{\sigma}_f DdS \tag{A4}$$

[*Rice*, 1980; *Li*, 1987], where $\bar{\sigma}_f$ is the average friction over the slip at a given location on the fault plane, i.e.,

$$\overline{\sigma}_f = \frac{1}{D}\int_D \sigma_f dD. \tag{A5}$$

Then, we approximate equation (A4) by

$$E_G + E_H \approx \bar{\bar{\sigma}}_f \bar{D}S, \tag{A6}$$

where $\bar{\bar{\sigma}}_f$ is now the spatial average of $\overline{\sigma}_f$ over the fault plane. Given the limited resolution of seismic data, we do not distinguish between $\overline{\sigma}_f$ and $\bar{\bar{\sigma}}_f$, and write

$$E_G + E_H \approx \overline{\sigma}_f \overline{D}S. \tag{A7}$$

In other words, $\overline{\sigma}_f$ is the average of σ_f over the slip and over the fault plane.

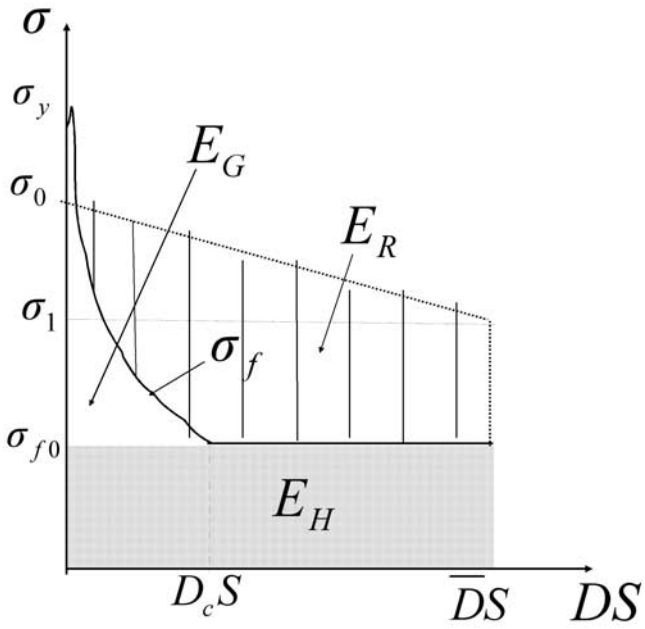

Figure B1. Undershoot model. The final stress on the fault is larger than the residual frictional stress on the fault. This could happen when the fault hits an obstacle and locks up prematurely.

[44] 3. The average of static stress drop is defined as

$$\Delta\overline{\sigma}_S = \frac{1}{S}\int_S \Delta\sigma_S dS, \tag{A8}$$

where $\Delta\sigma_S$ is the stress drop, and the area of this slip region is S. The integration is over the fault area, S. However, we approximate this by

$$\Delta\overline{\sigma}_S \approx C\mu\frac{\overline{D}}{\tilde{L}}, \tag{A9}$$

where $\tilde{L}$ is a characteristic rupture dimension, C is a geometric constant of order unity. For simplicity, we drop the bar on the stress drop and write

$$\Delta\sigma_S \approx C\mu\frac{\overline{D}}{\tilde{L}}. \tag{A10}$$

[45] Expressions (A3), (A7), and (A10) are used in this paper. Unfortunately, given the limited resolution of seismic data, we cannot fully assess the validity of these approximations. However, *Madariaga* [1977, 1979], *Rudnicki and Kanamori* [1981] and *Das* [1988] show that equation (A10) is a good approximation unless the variation of stress on the fault is extremely large. Similar arguments probably apply to equations (A3) and (A7), but it should be borne in mind that these uncertainties are inevitable in the use of macroscopic parameters.

Appendix B: Earthquakes With Radiation Efficiency Larger Than 1

[46] The radiation efficiency, η_R should be less than 1 by definition, but for a few earthquakes the computed η_R is larger than 1. There are two possibilities; either the estimates of radiated energy and/or stress drops are inaccurate, or the model we use to calculate η_R is inappropriate. Despite the careful corrections we applied, the poor knowledge of the attenuation structure of the Earth at higher frequencies could result in inaccuracies in the energy estimates. Also, as mentioned earlier, the estimates of static stress drop also have uncertainties. However, it is also possible that there is a stress undershoot (i.e., the final stress on the fault is larger than the residual frictional stress).

[47] In this case, from Figure B1, we can write

$$\begin{aligned}\eta_R = \frac{E_R}{E_R + E_G} &= \frac{E_R}{\Delta\sigma_S\overline{D}S/2 + (\sigma_1 - \sigma_{f0})\overline{D}S} \\ &= \frac{E_R/M_0}{\frac{\Delta\sigma_S}{2\mu}\left(1 + \frac{2(\sigma_1 - \sigma_{f0})}{\Delta\sigma_S}\right)} \\ &= \frac{\eta'_R}{\left(1 + \frac{2(\sigma_1 - \sigma_{f0})}{\Delta\sigma_S}\right)},\end{aligned}$$

where $\eta'_R = \dfrac{E_R/M_0}{\Delta\sigma_S/2\mu}$ is the radiation efficiency calculated from the radiated energy-to-moment ratio and strain drops. Thus

$$\eta'_R = \left(1 + \frac{2(\sigma_1 - \sigma_f)}{\Delta\sigma_S}\right)\eta_R, \tag{B1}$$

and hence if there is a stress undershoot, it is possible that $\eta'_R > 1$ and this could explain our observations. Moreover, if the rupture propagates as a slip pulse [*Heaton*, 1990] we would expect a stress undershoot. Some studies suggest that the Landers earthquake (1992) and the Northridge earthquake (1994) data are better explained by slip pulse models; however, the degree of undershoot is not determined well.

[48] **Acknowledgments.** This research was partially supported by NSF Cooperative Agreements EAR-9909371 and EAR-0125182 and also USGS-HQGR0035. We thank Kevin Mayeda and an anonymous reviewer for comments and suggestions that considerably improved our manuscript. This is contribution 8948 of the Caltech Division of Geological and Planetary Sciences.

References

Abercrombie, R., M. Antolik, K. Felzer, and G. Ekstrom (2001), The 1994 Java tsunami earthquake: Slip over a subducting seamount, *J. Geophys. Res.*, *106*, 6595–6607.

Antolik, M., D. Dreger, and B. Romanowicz (1996), Finite fault source study of the great 1994 deep Bolivia earthquake, *Geophys. Res. Lett.*, *23*, 1589–1592.

Barragan, B. E., G. M. Giaccio, and R. L. Zerbino (2001), Fracture and failure of thermally damaged concrete under tensile loading, *Mater. Struct.*, *34*, 312–319.

Boatwright, J., and G. L. Choy (1986), Teleseismic estimates of the energy radiated by shallow earthquakes, *J. Geophys. Res.*, *91*, 2095–2112.

Boore, D. M., and S. W. Dunbar (1977), Effect of the free surface on calculated stress drops, *Bull. Seismol. Soc. Am.*, *67*, 1661–1664.

Carlo, D. L., T. Lay, C. J. Ammon, and J. Zhang (1999), Rupture Process of the 1995 Antofagasta Subduction Earthquake (M_w = 8.1), *Pure Appl. Geophys.*, *154*, 677–708.

Choy, G. L., and J. Boatwright (1995), Global patterns of radiated energy and apparent stress, *J. Geophys. Res.*, *100*, 18,205–18,228.

Courboulex, F., S. K. Singh, J. F. Pacheco, and C. J. Ammon (1997), The 1995 Colima-Jalisco, Mexico, earthquake (M_w 8.0), A study of the rupture process, *Geophys. Res. Lett.*, *24*, 1019–1022.

Dahlen, F. A. (1977), The balance of energy in earthquake faulting, *Geophys. J. R. Astron. Soc.*, *48*, 239–261.

Das, S. (1988), Relation between average slip and average stress drop for rectangular faults with multiple asperities, *Bull. Seismol. Soc. Am.*, *78*, 924–930.

Der, Z. A. (1998), High frequency *P*- and *S*-wave attenuation in the Earth, *Pure Appl. Geophys.*, *153*, 273–310.
Dreger, D. S. (1994), Investigation of the rupture process of the 28 June 1992 Landers earthquake utilizing TERRASCOPE, *Bull. Seismol. Soc. Am.*, *84*, 713–724.
Escobedo, D., J. F. Pacheco, and G. Suarez (1998), Teleseismic body-wave analysis of the 9 October, 1995 (M_w = 8.0) Colima-Jalisco, Mexico, earthquake and its largest foreshock and aftershock, *Geophys. Res. Lett.*, *25*, 547–550.
Eshelby, J. D. (1969), The elastic field of a crack extending non-uniformly under general anti-plane loading, *J. Mech. Phys. Solids*, *17*, 177–199.
Fossum, A. F., and L. B. Freund (1975), Nonuniformly moving shear crack model of a shallow focus earthquake mechanism, *J. Geophys. Res.*, *80*, 3343–3347.
Freund, L. B. (1972), Crack propagation in an elastic solid subjected to general loading. II. Nonuniform rate of extension, *J. Mech. Phys. Solids*, *20*, 141–152.
Frolich, C. (1989), The nature of deep-focus earthquakes, *Annu. Rev. Earth Planet. Sci.*, *17*, 227–254.
Giardini, D. (1988), Frequency distribution and quantification of deep earthquakes, *J. Geophys. Res.*, *93*, 2095–2105.
Goes, S., and J. Ritsema (1995), A broadband *P* wave analysis of the large deep Fiji Island and Bolivia earthquakes of 1994, *Geophys. Res. Lett.*, *22*, 2249–2252.
Goes, S., L. J. Ruff, and N. W. Winslow (1997), The complex rupture process of the 1996 deep Flores, Indonesia earthquake (M_w 7.9) from teleseismic *P*-waves, *Geophys. Res. Lett.*, *24*, 1295–1298.
Green, H. W., II, and P. C. Burnley (1989), A new self-organizing mechanism for deep-focus earthquakes, *Nature*, *341*, 733–737.
Green, H. W., II, and H. Houston (1995), The mechanics of deep earthquakes, *Annu. Rev. Earth Planet. Sci.*, *23*, 169–213.
Griggs, D. T., and D. W. Baker (1968), The origin of deep-focus earthquakes, in *Properties of Matter Under Unusual Conditions: In Honor of Edward Teller's 60th Birthday*, edited by M. Hans and F. Sidney, pp. 23–42, John Wiley, Hoboken, N. J.
Guatteri, M., and P. Spudich (2000), What can strong motion data tell us about slip-weakening fault-friction laws?, *Bull. Seismol. Soc. Am.*, *90*, 98–116.
Gutenberg, B., and C. F. Richter (1938), Depth and geographical distribution of deep-focus earthquakes, *Geol. Soc. Am. Bull.*, *49*, 249–288.
Gutenberg, B., and C. F. Richter (1939), Depth and geographical distribution of deep-focus earthquakes, *Geol. Soc. Am. Bull.*, *50*, 1511–1528.
Hartog, J. R., and S. Y. Schwartz (1996), Directivity analysis of the December 28, 1994 Sanriku-oki earthquake (M_w = 7.7), Japan, *Geophys. Res. Lett.*, *23*, 2037–2040.
Heaton, T. (1990), Evidence for and implications of self-healing pulses of slip in earthquake rupture, *Phys. Earth Planet. Inter.*, *64*, 1–20.
Heki, K., S. Miyazaki, and T. Hiromichi (1997), Silent fault slip following an interplate thrust earthquake at the Japan trench, *Nature*, *386*(6625), 595–598.
Hurukawa, N. (1998), The 1995 Off-Etorofu earthquake: Joint relocation of foreshocks, the mainshock, and aftershocks and implications for the earthquake nucleation process, *Bull. Seismol. Soc. Am.*, *88*, 1112–1126.
Husseini, M. I. (1977), Energy balance for motion along a fault, *Geophys. J. R. Astron. Soc.*, *49*, 699–714.
Ide, S., and M. Takeo (1997), Determination of constitutive relations of fault slip based on seismic wave analysis, *J. Geophys. Res.*, *102*, 27,379–27,391.
Ihmle, P. F. (1996), Monte Carlo slip inversion in the frequency domain: Application to the 1992 Nicaragua slow earthquake, *Geophys. Res. Lett.*, *23*, 913–916.
Ihmle, P. F., J. Gomez, P. Heinrich, and S. Guibourg (1998), The 1996 Peru tsunamigenic earthquake: Broadband source processes, *Geophys. Res. Lett.*, *25*, 2691–2694.
Janssen, C., F. C. Wagner, A. Zang, and G. Dresen (2001), Fracture process zone in granite: A microstructural analysis, *Int. J. Earth Sci.*, *90*, 46–59.
Ji, C., D. J. Wald, and D. V. Helmberger (2002), Source description of the 1999 Hector Mine, California earthquake; part II: Complexity of slip history, *Bull. Seismol. Soc. Am.*, *92*, 1208–1227.
Ji, C., D. V. Helmberger, D. J. Wald, and K.-F. Ma (2003), Slip history and dynamic implications of the 1999 Chi-Chi, Taiwan, earthquake, *J. Geophys. Res.*, *108*(B9), 2412, doi:10.1029/2002JB001764.
Johnson, J. M., Y. Tanioka, K. Satake, and L. J. Ruff (1995), Two 1993 Kamchatka earthquakes, *Pure Appl. Geophys.*, *144*, 633–647.
Kajiura, K. (1970), Tsunami source, energy and the directivity of wave radiation, *Bull. Earthquake Res. Inst. Tokyo Univ.*, *48*, 835–869.
Kanamori, H. (1972), Mechanism of tsunami earthquakes, *Phys. Earth Planet. Inter.*, *6*, 346–359.
Kanamori, H. (1994), Mechanics of Earthquakes, *Annu. Rev. Earth Planet. Sci.*, *22*, 207–237.
Kanamori, H., and T. Heaton (2000), Microscopic and macroscopic physics of earthquakes, in *Geocomplexity and the Physics of Earthquakes*, *Geophys. Monogr. Ser.*, vol. 120, edited by J. Rundle, D. L. Turcotte, and W. Klein, pp. 147–163, AGU, Washington, D. C.
Kanamori, H., and M. Kikuchi (1993), The 1992 Nicaragua earthquake: A slow tsunami earthquake associated with subducted sediments, *Nature*, *361*, 714–716.
Kanamori, H., D. L. Anderson, and T. H. Heaton (1998), Frictional melting during the rupture of the 1994 Bolivian Earthquake, *Science*, *279*, 839–842.
Karato, S., M. R. Riedel, and D. A. Yuen (2001), Rheological structure and deformation of subducted slabs in the mantle transition zone: Implications for mantle circulation and deep earthquakes, *Phys. Earth Planet. Inter.*, *127*, 83–108.
Kaverina, A., D. Dreger, and M. Antolik (1998), Source process of the 21 April, 1997 Santa Cruz Island earthquake (M_w 7.8), *Geophys. Res. Lett.*, *25*, 4027–4030.
Kikuchi, M. (1992), Strain drop and apparent strain for large earthquakes, *Tectonophysics*, *211*, 107–113.
Kikuchi, M., and H. Kanamori (1994), The mechanism of the deep Bolivia earthquake of June 9, 1994, *Geophys. Res. Lett.*, *21*, 2341–2344.
Kikuchi, M., and H. Kanamori (1995a), The Shikotan earthquake of October 4, 1994: Lithospheric earthquake, *Geophys. Res. Lett.*, *22*, 1025–1028.
Kikuchi, M., and H. Kanamori (1995b), Source characteristics of the 1992 Nicaragua tsunami earthquake inferred from teleseismic body waves, *Pure Appl. Geophys.*, *144*, 441–453.
Kirby, S. H., W. B. Durham, and L. A. Stern (1991), Mantle phase changes and deep-earthquake faulting in subducting lithosphere, *Science*, *252*, 216–225.
Knopoff, L. (1958), Energy release in earthquakes, *Geophys. J.*, *1*, 44–52.
Kostrov, B. V. (1966), Unsteady propagation of longitudinal shear cracks, *J. Appl. Math. Mech. Engl. Transl.*, *30*, 1241–1248.
Kostrov, B. V. (1974), Seismic moment and energy of earthquakes, and seismic flow of rock (translated to English), *Izv. Earth Phys.*, *1*, 23–40.
Lawn, B. (1993), *Fracture of Brittle Solids*, 2nd ed., 378 pp., Cambridge Univ. Press, New York.
Li, V. C. (1987), Mechanics of shear rupture applied to earthquake zones, in *Fracture Mechanics of Rock*, edited by B. Atkinson, pp. 351–428, Academic, San Diego, Calif.
Madariaga, R. (1977), Implications of stress-drop models of earthquakes for the inversion of stress drop from seismic observations, *Pure Appl. Geophys.*, *115*, 301–316.
Madariaga, R. (1979), On the relation between seismic moment and stress drop in the presence of stress and strength heterogeneity, *J. Geophys. Res.*, *84*, 2243–2250.
Mai, P. M., and G. C. Beroza (2000), Source scaling properties from finite-fault-rupture models, *Bull. Seismol. Soc. Am.*, *90*, 604–615.
Mayeda, K., and W. R. Walter (1996), Moment, energy, stress drop, and source spectra of western United States earthquakes from regional coda envelopes, *J. Geophys. Res.*, *101*, 11,195–11,208.
McGarr, A., and J. B. Fletcher (2001), A method for mapping apparent stress and energy radiation applied to the 1994 Northridge earthquake fault-zone-revisited, *Geophys. Res. Lett.*, *28*, 3529–3532.
Meade, C., and R. Jeanloz (1991), Deep focus earthquakes and recycling of water into the earth's mantle, *Science*, *252*, 68–72.
Mendoza, C., and E. Fukuyama (1996), The July 12, 1993, Hokkaido-Nansei-Oki, Japan, earthquake: Coseismic slip pattern from strong-motion and teleseismic recordings, *J. Geophys. Res.*, *101*, 791–801.
Mendoza, C., and S. Hartzell (1999), Fault-slip distribution of the 1995 Colima-Jalisco, Mexico, earthquake, *Bull. Seismol. Soc. Am.*, *89*, 1338–1344.
Mott, N. F. (1948), Brittle fractures in mild-steel plates-II, *Engineering*, *165*, 16–18.
Nakayama, W., and M. Takeo (1997), Slip history of the 1994 Sanriku-Haruka-Oki, Japan, earthquake deduced from strong-motion data, *Bull. Seismol. Soc. Am.*, *87*, 918–931.
Nazareth, J. (2002), The structure of and the distribution of earthquakes within the crust of Southern California, Ph.D. thesis, Calif. Inst. of Technol., Pasadena, Calif.
Negishi, H., J. Mori, T. Sato, R. Singh, S. Kumar, and N. Hirata (2002), Size and orientation of the fault plane for the 2001 Gujarat, India earthquake (Mw7.7) from aftershock observations: A high stress drop event, *Geophys. Res. Lett.*, *29*(20), 1949, doi:10.1029/2002GL015280.
Ogawa, M. (1990), Shear instability in a viscoelastic material as the cause of deep focus earthquakes, *J. Geophys. Res.*, *92*, 13,801–13,810.
Olson, K. B., R. Madariaga, and R. J. Archuleta (1997), Three-dimensional simulation of the 1992 Landers earthquake, *Science*, *278*, 834–838.
Ozawa, S. (1996), Geodetic inversion for the fault model of the 1994 Shikotan earthquake, *Geophys. Res. Lett.*, *23*, 2009–2012.

Pacheco, J., et al. (1997), The October 9, 1995 Colima-Jalisco, Mexico earthquake (M_w 8): An aftershock study and comparison of this earthquake with those of 1932, *Geophys. Res. Lett.*, *24*, 2223–2226.

Parsons, I. D., J. F. Hall, and G. A. Lyzenga (1988), Relationships between the average offset and the stress drop for two- and three-dimensional faults, *Bull. Seismol. Soc. Am.*, *78*, 931–945.

Polet, J., and H. Kanamori (2000), Shallow subduction zone earthquakes and their tsunamigenic potential, *Geophys. J. Int.*, *142*, 684–702.

Poliakov, A. N. B., R. Dmowska, and J. R. Rice (2002), Dynamic shear rupture interactions with fault bends and off-axis secondary faulting, *J. Geophys. Res.*, *107*(B11), 2295, doi:10.1029/2001JB000572.

Ravichandar, K., and W. G. Knauss (1984), An experimental investigation into dynamic fracture. 3. On steady-state crack-propagation and crack branching, *Int. J. Fract.*, *26*, 141–154.

Reugg, J. C., et al. (1996), The M_w = 8.1 Antofagasta (North Chile) earthquake of July 30, 1995: First results from teleseismic and geodetic data, *Geophys. Res. Lett.*, *23*, 917–920.

Rice, J. R. (1980), The mechanics of earthquake rupture, in *Physics of the Earth's Interior*, edited by A. M. Dziewonski and E. Boschi, pp. 555–649, North-Holland, New York.

Rosakis, A. J., and A. T. Zehnder (1985), On the dynamic fracture of structural metals, *Int. J. Fract.*, *27*, 169–186.

Rudnicki, J. W., and H. Kanamori (1981), Effects of fault interaction on moment, stress drop, and strain energy release, *J. Geophys. Res.*, *86*, 1785–1793.

Sato, T., K. Imanishi, and M. Kosuga (1996), Three-stage rupture process of the 28 December 1994 Sanriku-Oki earthquake, *Geophys. Res. Lett.*, *23*, 33–36.

Scholz, C. H. (1990), *The Mechanics of Earthquake Faulting*, 438 pp., Cambridge Univ. Press, New York.

Schwartz, S. (1999), Noncharacteristic behavior and complex recurrence of large subduction zone earthquakes, *J. Geophys. Res.*, *104*, 23,111–23,125.

Silver, P. G., S. L. Beck, T. C. Wallace, C. Meade, S. C. Myers, D. E. James, and R. Kuehnel (1995), Rupture characteristics of the deep Bolivian earthquake of 9 June 1994 and the mechanism of deep-focus earthquakes, *Science*, *268*, 69–73.

Somerville, P., K. Irikura, R. Graves, S. Sawada, D. J. Wald, N. Abrahamson, Y. Iwasaki, T. Kagawa, N. Smith, and A. Kowada (1999), Characterizing crustal earthquake slip models for the prediction of strong ground motion, *Seismol. Res. Lett.*, *70*(1), 59–80.

Swenson, J. L., and S. L. Bilek (1999), Source characteristics of the 12 November 1996 M_w 7.7 Peru subduction zone earthquake, *Pure Appl. Geophys.*, *154*, 731–751.

Takeo, M., S. Ide, and Y. Yoshida (1993), The 1993 Kushiro-Oki, Japan, earthquake: A high stress drop event in a subducting slab, *Geophys. Res. Lett.*, *23*, 2607–2610.

Tanioka, Y., and F. I. Gonzalez (1998), The Aleutian earthquake of June 10, 1996 (M_w 7.9) ruptured parts of both the Adreanof and Delarof segments, *Geophys. Res. Lett.*, *25*, 2245–2248.

Tanioka, Y., and K. Satake (1996), Tsunami generation by horizontal displacement of ocean bottom, *Geophys. Res. Lett.*, *23*, 861–864.

Tanioka, Y., K. Satake, and L. J. Ruff (1995), Total analysis of the 1993 Hokkaido Nansei-oki earthquake using seismic wave, tsunami, and geodetic data, *Geophys. Res. Lett.*, *22*, 9–12.

Tanioka, Y., L. J. Ruff, and K. Satake (1997), What controls the lateral variation of large earthquake occurrence along the Japan trench?, *Island Arc*, *6*, 261–266.

Thio, H. K., and H. Kanamori (1996), Source complexity of the 1994 Northridge earthquake and its relation to aftershock mechanisms, *Bull. Seismol. Soc. Am.*, *86*, S84–S92.

Tibi, R., C. H. Estabrook, and G. Bock (1999), The 1996 June 17 Flores Sea and the March 9 Fiji-Tonga earthquakes: Source processes and deep earthquake mechanisms, *Geophys. J. Int.*, *138*, 625–642.

Tibi, R., G. Bock, M. Xia, M. Baumbach, and H. Grosser (2001), Rupture processes of the 1999 August 17 Izmit and November 12 Duzce (Turkey) earthquakes, *Geophys. J. Int.*, *144*, F1–F7.

Tibi, R., G. Bock, and D. A. Wiens (2003), Source characteristics of large deep earthquakes: Constraint on the faulting mechanism at great depths, *J. Geophys. Res.*, *108*(B2), 2091, doi:10.1029/2002JB001948.

Venkataraman, A. (2002), Investigating the mechanics of earthquakes using macroscopic seismic parameters, Ph.D. thesis, Calif. Inst. of Technol., Pasadena, Calif. (http://etd.caltech.edu/etd/available/etd-06132002-094224)

Venkataraman, A., and H. Kanamori (2004), Effect of directivity on estimates of radiated seismic energy, *J. Geophys. Res.*, *109*, B04301, doi:10.1029/2003JB002548.

Venkataraman, A., L. Rivera, and H. Kanamori (2002), Radiated energy from the 16 October 1999 Hector Mine Earthquake: Regional and teleseismic estimates, *Bull. Seismol. Soc. Am.*, *92*, 1256–1266.

Wald, D. J., T. H. Heaton, and K. W. Hudnut (1996), The slip history of the 1994 Northridge, California earthquake determined from strong-motion, teleseismic, GPS, and leveling data, *Bull. Seismol. Soc. Am.*, *86*, S49–S70.

Wha, S. S. (1998), The 1997 Kamchatka earthquake, *Individual Stud. Participants Int. Inst. Seismol. Earthquake Eng.*, *34*, 91–99.

Wiens, D. (2001), Seismological constraints on the mechanism of deep earthquakes: Temperature of deep earthquake source properties, *Phys. Earth Planet. Inter.*, *127*, 145–163.

Wiens, D., and H. J. Gilbert (1996), Effect of slab temperature on deep-earthquake aftershock productivity and magnitude-frequency relationships, *Nature*, *384*, 153–156.

Wu, L.-R., and W.-P. Chen (2001), Rupture of the large (M_w 7.8), deep earthquake of 1973 beneath the Japan sea with implications for seismogenisis, *Bull. Seismol. Soc. Am.*, *91*, 102–111.

Yagi, Y., and M. Kikuchi (2000), Source rupture process of the Kocaeli, turkey, earthquake of August 17, 1999, obtained by joint inversion of near-field data and teleseismic data, *Geophys. Res. Lett.*, *27*, 1969–1972.

Yoshiaka, S., and Y. Tokunaga (1998), Numerical simulation of displacement and stress fields associated with the 1993 Kushiro-oki, Japan, earthquake, *Pure Appl. Geophys.*, *152*, 443–464.

Zeng, Y., and J. G. Anderson (1996), A composite source model of the 1994 Northridge earthquake using genetic algorithms, *Bull. Seismol. Soc. Am.*, *86*, S71–S83.

H. Kanamori, Seismological Laboratory, California Institute of Technology, Pasadena, CA 91125, USA.

A. Venkataraman, Department of Geophysics, Stanford University, Stanford, CA 94305, USA. (anupamav@pangea.stanford.edu)

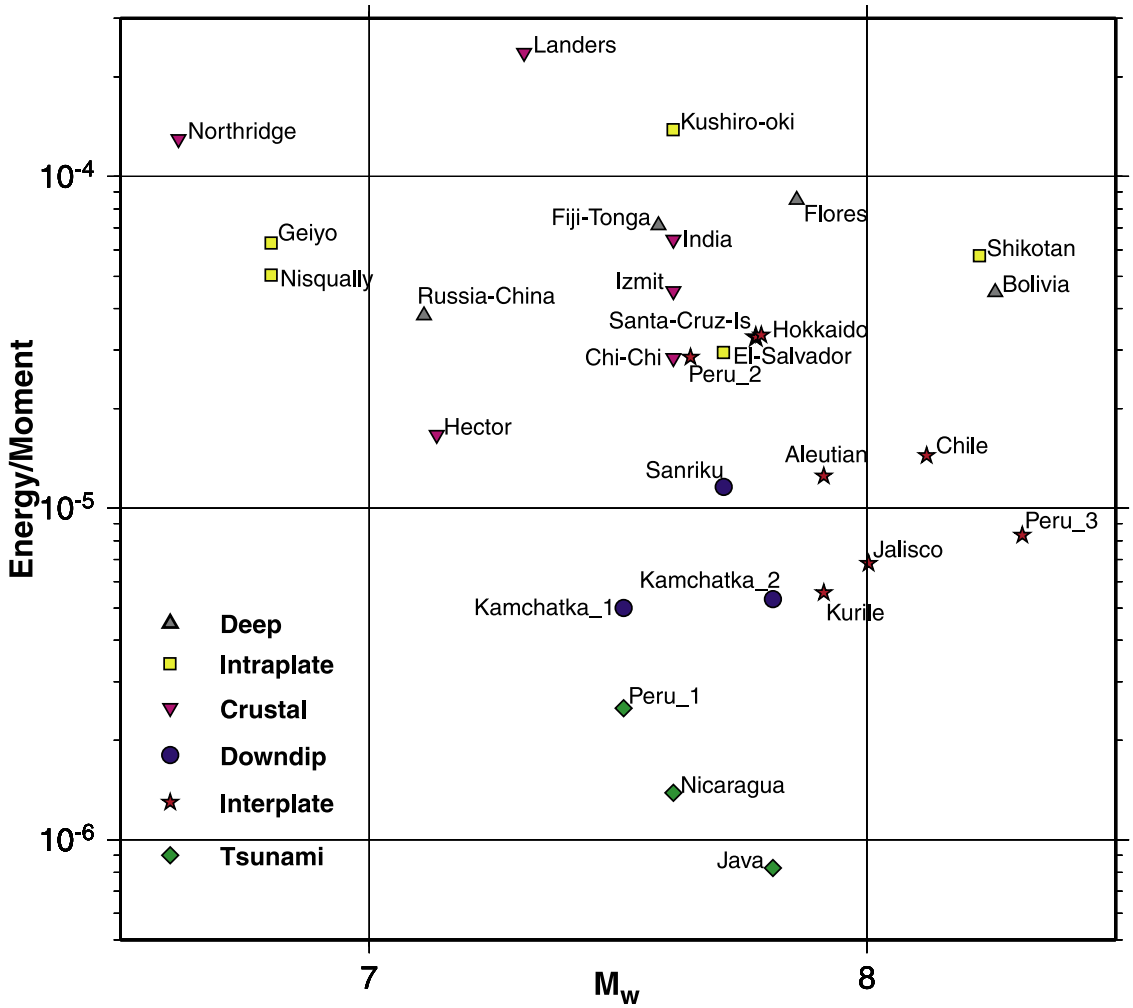

Figure 5. The computed energy-to-moment ratios plotted as a function of moment magnitude. The different symbols show different types of earthquakes as described in the legend. It is observed that tsunami earthquakes have the smallest energy-to-moment ratios, and crustal and deep earthquakes have the largest energy-to-moment ratios.

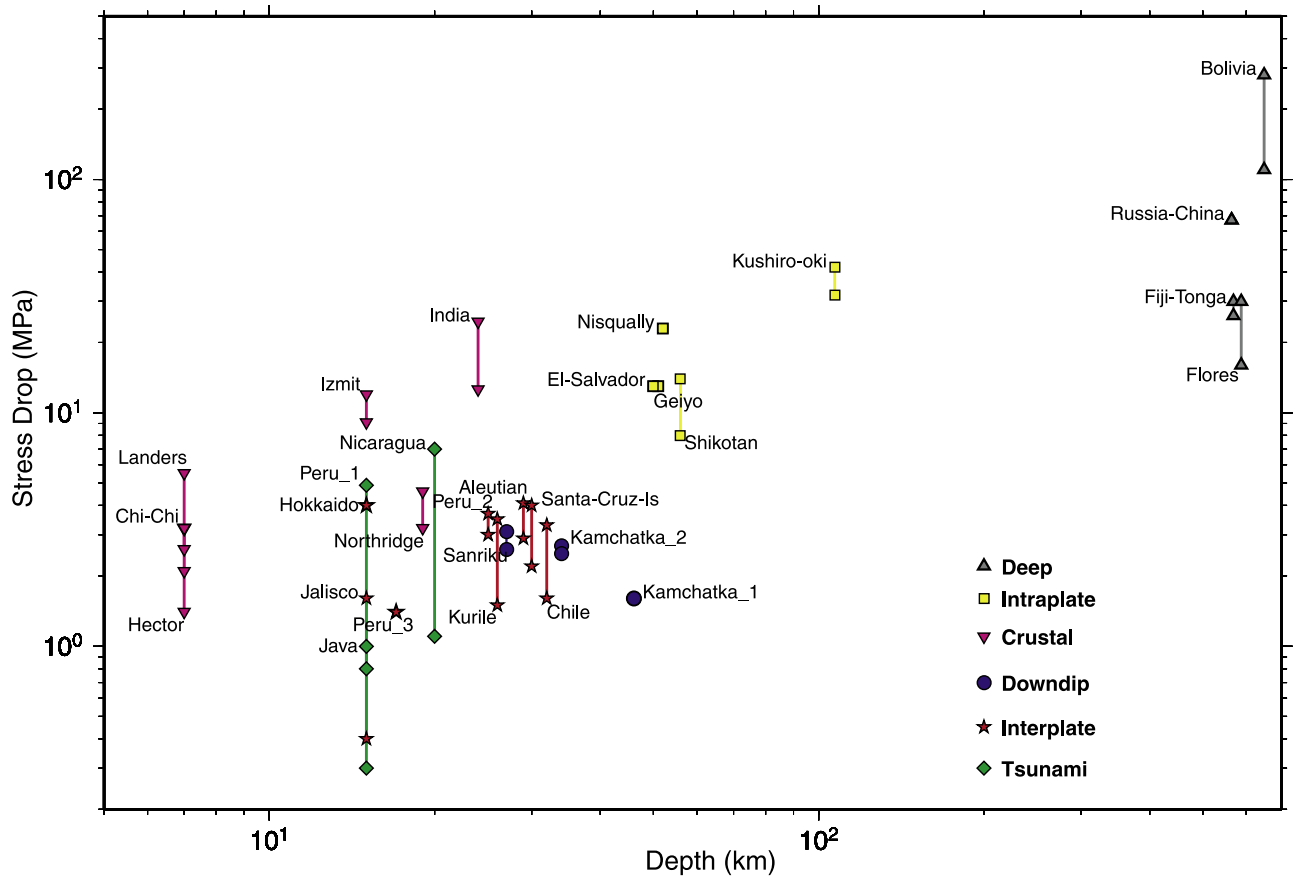

Figure 7. Static stress drop plotted as a function of depth for the different types of earthquakes studied.

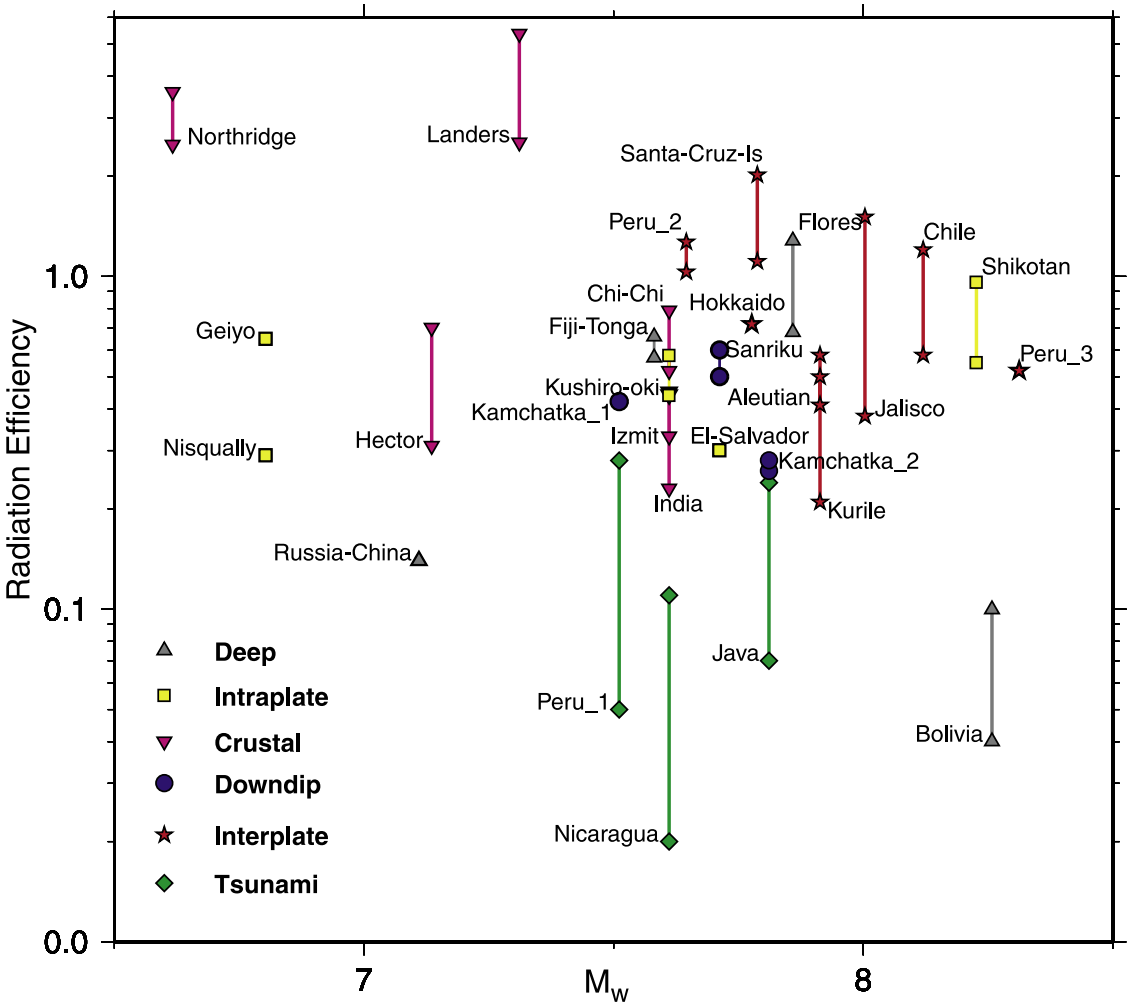

Figure 8. Radiation efficiencies determined from the radiated energy-to-moment ratios are plotted as a function of moment magnitude. The different symbols show different types of earthquakes as described in the legend. Most earthquakes have radiation efficiencies greater than 0.25, but tsunami earthquakes and two of the deep earthquakes (the Bolivia earthquake and the Russia-China earthquake) have small radiation efficiencies.

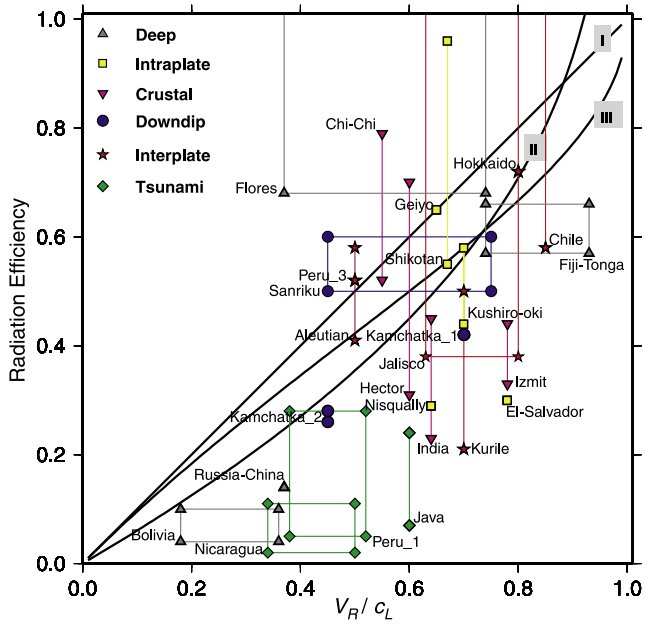

Figure 9. Radiation efficiencies determined from the radiated energy-to-moment ratios and estimates of static stress drop plotted against the estimates of the ratio of rupture velocity to shear wave velocity obtained from literature. Symbols are the same as before; for comparison, the theoretical curves relating radiation efficiency to rupture velocity for Mode I, Mode II, and Mode III cracks have also been plotted.